



Vertical redistribution of moisture and aerosol in orographic mixed-phase clouds

Annette K. Miltenberger^{1,2}, Paul R. Field^{1,3}, and Adrian H. Hill³

¹Institute of Climate and Atmospheric Science, School of Earth and Environment, University of Leeds, United Kingdom

²Institute for Atmospheric Physics, Johannes Gutenberg-University Mainz, Germany

³MetOffice, Exeter, United Kingdom

Correspondence: Annette K. Miltenberger (amiltenb@uni-mainz.de)

Abstract. Orographic wave clouds offer a natural laboratory to investigate cloud microphysical processes and their representation in atmospheric models. Wave clouds impact the larger-scale flow by the vertical redistribution of moisture and aerosol. Here we use detailed cloud microphysical observations from the ICE-L campaign to evaluate the recently developed Cloud Aerosol Interacting Microphysics (CASIM) module in the Met Office Unified Model (UM) with a particular focus on different parameterisations for heterogeneous freezing. Modelled and observed thermodynamic and microphysical properties agree very well (deviation of air temperature < 1 K, specific humidity < 0.2 g kg⁻¹, vertical velocity < 1 ms⁻¹, cloud droplet number concentration < 40 cm⁻³), with the exception of an overestimated total condensate content and a too long sedimentation tail. The accurate reproduction of the environmental thermodynamic and dynamical wave structure enables the model to reproduce the right cloud in the right place and at the right time. All heterogeneous freezing parameterisations except Atkinson et al. (2013) perform reasonably well, with the best agreement in terms of the temperature dependency of ice crystal number concentrations for the parameterisations of DeMott et al. (2010) and Tobo et al. (2013). The novel capabilities of CASIM allowed testing of the impact of assuming different soluble fractions on dust particles on immersion freezing, but this is found to only have a minor impact on hydrometeor mass and number concentrations.

The simulations were further used to quantify the modification of moisture and aerosol profiles by the wave cloud. The changes in both variables are on order of 15 % of their upstream values, but the modifications have very different vertical structures for the two variables. Using a large number of idealised simulations we investigate how the induced changes depend on the wave period (100 – 1800 s), cloud-top temperature (-15 to -50 °C) and cloud thickness (1 – 5 km) and propose a conceptual model to describe these dependencies.



1 Introduction

The advent of (sub-)kilometre scale numerical weather prediction models in recent years has strongly improved the prediction of clouds and precipitation (e.g. Clark et al., 2016). However, simplification in the representation of cloud microphysical processes and incomplete physical understanding of some key processes result in fairly large uncertainties in the representation of individual cloud microphysical processes, which also impact the macroscopic appearance of clouds, precipitation formation and cloud evolution (e.g. Muhlbauer et al., 2010; Johnson et al., 2015). To improve the representation of cloud microphysical processes and to reduce the associated uncertainty, the combination of model simulations with detailed observational data from dedicated field campaigns is of fundamental importance alongside the careful investigation of individual processes in the laboratory. Clouds forming in laminar flow in the vicinity of significant topography, so-called orographic wave clouds, have been suggested as natural laboratories to investigate cloud processes under ambient atmospheric conditions (e.g. Heymsfield and Miloshevich, 1993; Field et al., 2001; Muhlbauer and Lohmann, 2009). In contrast to convective cloud fields, the quasi-stationary, laminar flow provides well-constrained thermodynamic environment and dynamic forcing and allows for direct comparisons between observations and model results (e.g. Heymsfield and Miloshevich, 1993; Eidhammer et al., 2010; Field et al., 2012).

Orographic clouds known to be important for weather and climate, as they occur frequently in mountainous regions (e.g. Grubisic and Billings, 2008; Vosper et al., 2013), modify regional precipitation patterns (e.g. Sawyer, 1956; Smith et al., 2015) and influence radiative fluxes (e.g. Joos et al., 2008). Most studies on orographic clouds have focussed on their contribution to surface precipitation and its distribution, which has been investigated in a large number of idealised and realistic simulations with models of various complexity (e.g. Houze, 2012; Miltenberger et al., 2015; Henneberg et al., 2017). It has been shown that depending on the upstream conditions and the shape of the topography different cloud microphysical processes dominate the precipitation formation (e.g. Jiang and Smith, 2003; Colle and Zeng, 2004) and varying ambient aerosol concentrations can modify precipitation amounts and patterns (e.g. Muhlbauer et al., 2010; Zubler et al., 2011; Xiao et al., 2015). Precipitation formation does not only result in a vertical redistribution of moisture, but also a vertical transport of aerosol particles, which are incorporated into hydrometeors during cloud droplet or ice crystal nucleation (nucleation scavenging) or by aerosol-hydrometeor collisions (impaction scavenging) (e.g. Xue et al., 2012; Pousse-Nottelmann et al., 2015). However, not all aerosol particles incorporated into hydrometeors are removed to the surface, as a significant fraction of condensate evaporates before reaching the ground and the associated aerosol particles are released upon evaporation (or sublimation) (e.g. Xue et al., 2012; Pousse-Nottelmann et al., 2015). The resulting modification of the vertical profile of aerosol number concentration and to a lesser degree also changes in their chemical composition have been shown to modify surface precipitation from subsequently forming clouds, although these changes are smaller than the impact of varying upstream humidity or aerosol number concentration (Xue et al., 2012).

While orographic clouds producing (large) amounts of precipitation are very relevant in socio-economic terms, isolated wave clouds in the middle troposphere, which do not produce surface precipitation, are better suited to study the basic mixed-phase cloud processes of heterogeneous freezing, depositional growth, hydrometeor sedimentation and aerosol transport. In con-



trast to thicker orographic clouds, the collision-coalescence process is less important and the interactions between air parcels travelling through the clouds at different altitudes is minimal. Also, their smaller horizontal and vertical extent implies that representative observations are obtained more easily. One particular question, for which observations in isolated mid-tropospheric mixed-phase wave clouds has been instrumental, is the glaciation of clouds. The formation of ice in all mixed-phase clouds, not only orographic wave clouds, plays a crucial role for the efficiency of precipitation formation (as already pointed out in early studies by Bergeron (1935) and Findeisen (2015)) and the cloud optical properties (e.g. Joos et al., 2014; Vergara-Temprado et al., 2018).

In the atmosphere ice forms either via homogeneous freezing of solution droplets at temperature colder than about -35°C or at warmer temperatures through the mediation of certain aerosol particles, which are called ice nucleating particles (INP). Aircraft observations in orographic wave clouds have demonstrated the large increase in ice crystal number concentration due to the onset of homogeneous freezing at cold cloud top temperatures: For example, Heymsfield and Miloshevich (1993) showed that ice crystal concentrations of $\sim 60\text{ cm}^{-3}$ observed at temperatures colder than -35°C in wave clouds over the central United States are consistent with box-model predictions assuming homogeneous freezing. Ice crystal concentrations at warmer temperatures were below the detection limit. Similarly, for wave clouds over Scandinavia Field et al. (2001) found homogeneous freezing to be dominant at temperatures colder than -35°C , while ice at warmer temperatures was most likely formed via immersion or contact nucleation, i.e. freezing mechanisms requiring INPs. Ice crystal number concentrations at these warmer temperatures has been observed to correlated with the presence of large aerosol particles (Baker and Lawson, 2006; Eidhammer et al., 2010) and chemical analysis of ice crystal residual found predominantly mineral dust with some contributions from organics and salts, which are known to be efficient INPs (e.g. Targino et al., 2006; Pratt et al., 2010). Depending on whether INPs are incorporated before or during the freezing event, different heterogeneous freezing mechanisms are distinguished. In mixed-phase orographic clouds immersion freezing, i.e. INPs acting first as cloud condensation nuclei and later initiating the freezing of the cloud droplets, is likely the dominant freezing mechanism according to model-based (Hande and Hoose, 2017) analysis and comparison between parcel model simulations and observations (Field et al., 2001; Eidhammer et al., 2010). However, Cotton and Field (2002) could not completely reconcile box-model simulations using known freezing mechanisms with observations of hydrometeor number concentrations and mass mixing ratios.

The representation of heterogeneous freezing in numerical models relies on empirical relationships involving aerosol number concentrations and temperatures, because the fundamental processes of the ice nucleation process and those determining the efficiency of specific aerosol particles to act as INP are not yet understood. Several empirical formulation of heterogeneous (immersion) freezing have been proposed: Early parameterisations such as Meyers et al. (1992) are solely based on ambient air temperature, while later parameterisations additionally take into account the number concentration of large ($> 0.5\ \mu\text{m}$) aerosol particles (e.g. DeMott et al., 2010; Tobo et al., 2013; DeMott et al., 2015). The main difference between the latter parameterisations is the geographic regions, in which the underlying observations were made, and hence they likely represent different chemical and/or mineralogical compositions of the INP population. Other recent parameterisations use estimates of the temperature-dependent number of active sites on specific materials and the surface area of the aerosol population to predict the number of INPs at a given temperature (Niemand et al., 2012; Atkinson et al., 2013). Again the main difference between



the parameterisations is the materials, for which the number of active sites was determined. It is not clear how the different parameterisations affect cloud properties and whether the difference between the parameterisations can be directly assessed with observations of ice crystal number concentrations.

Previous work has demonstrated the usefulness of observations in orographic clouds to investigate cloud microphysical processes. However, detailed cloud-microphysical analysis in models was limited to box-, column or idealised two-dimensional simulations. Here we use observations in isolated, mid-level wave clouds during the ICE-L campaign to assess the performance of the recently developed Cloud-Aerosol Interacting Module (CASIM) in three-dimensional simulations with Met Office Unified Model (UM), i.e. a non-hydrostatic model used for operational weather prediction. The objectives of the present work are in particular:

- 100 – Is the numerical weather prediction model able to capture the thermodynamic conditions and wave cloud dynamics with sufficient accuracy, i.e. the right cloud in the right place at the right time, to allow for a direct comparison of cloud microphysical properties between model and observations?
- Can observations of the vertical variation in ice crystal number concentration be used to assess the validity of different heterogeneous freezing parameterisations?
- 105 – How large is the modification of the water vapour and aerosol profiles by the wave cloud? How does the downward transport of water vapour and aerosols depend on the upstream thermodynamic conditions? And under which conditions is the downward flux largest, i.e. can be best observed in future campaigns?

The analysis focusses on a wave cloud over the Central United States probed with the National Science Foundation (NSF) C-130 aircraft (17th November 2007, RF03) during the ICE-L campaign Heymsfield et al. (2011); Pratt et al. (2010). Data from ICE-L has been used to investigate the relationship between upstream INP measurements and ice crystal number concentrations (Eidhammer et al., 2010; Field et al., 2012), the depositional growth of ice crystals (Heymsfield et al., 2011) and to investigate the impact of using adaptive ice crystal habits in idealised model simulations (Dearden et al., 2012). The chemical analysis of cloud droplet and ice crystal residuals by Pratt et al. (2010) indicated that INPs active in the observed wave clouds are most likely mineral dust internally mixed with a significant salt component, as may be expected from aerosols emitted from playas in the Central United States.

Details on the observations, models and their set-up are provided in the following section. In section 3 we present the comparison of observed wave cloud properties to the results from high-resolution simulations with the Met Office UM with a specific focus on the vertical gradient in ice crystal number concentration (sec. 3.3). A Lagrangian analysis of the simulations provides insight into the modification of humidity and aerosol profiles by the wave cloud (section 4.1). The dependence of amplitude and shape of this modification on the gravity wave length and upstream thermodynamic conditions determining cloud top temperature and cloud thickness is assessed with additional idealised simulations in section 4.2. Finally, section 5 summarises the results and discusses implications for future aircraft observations in orographic wave clouds to constrain mixed-phase cloud microphysics.



125 2 Data and Methods

2.1 Observational data from ICE-L

Detailed in-situ cloud microphysical observations in orographic wave clouds are available from the Ice in Clouds Experiment (ICE-L) conducted over the central US in November 2007 (e.g. Eidhammer et al., 2010; Heymsfield et al., 2011; Field et al., 2012). Various instruments onboard of the National Science Foundation (NSF) C-130 aircraft provide information of aerosol, cloud and ice populations in the observed mixed-phase clouds. Details on the instrumentation can be found in Heymsfield et al. (2011) for hydrometeor and aerosol size distributions and Pratt et al. (2010) for the aerosol chemical composition. Here we focus on a wave cloud observed on 16th November 2007 (RF03), for which observations from three different altitudes are available within a time interval of roughly 40 min. For the model evaluation, we use the King liquid water probe for total liquid water content, the 2D-C probe for ice water content and number concentrations, the CDP (cloud droplet probe) for cloud number concentrations, the tuneable diode laser hygrometer (TDL) for humidity measurements and aerosol size distributions from the Ultra High Sensitivity Aerosol Spectrometer for size-resolved number concentrations (UHSAS). As in Field et al. (2012) we restrict 2D-C data to particles larger than 125 μm and correct the TDL humidity such that it is consistent with water saturation in the regions with a liquid water content (from the King liquid water probe) larger than 0.02 g m^{-3} . Further details on the data and its post-processing can be found in Field et al. (2012).

140 2.2 The Unified Model

We use the Unified Model (UM), the numerical weather prediction model developed by the MetOffice and used for operational forecasting in the UK, to conduct simulations of the wave cloud observed during research flight 3 of the ICE-L campaign (16th November 2007). A global simulation (UM vn10.8, GA6 configuration, N512 resolution, Walters et al. (2017)) starting from the operational analysis at 12 UTC on 16th November 2007 provides the initial and lateral boundary conditions for regional model simulations. Two regional nests are used, the first with a horizontal grid spacing of 1 km and the second with a grid spacing of 250 m. Both nests are centred at the location of the observed wave cloud (42.116 °N, -105.1 °E). The analysis presented in this paper focusses on the innermost nest. In the vertical we use a stretched vertical coordinate system with 140 levels, which provides a vertical resolution of 130 – 200 m at the altitude of the observed cloud. Mass conservation is enforced in the regional simulations (Aranami et al., 2014, 2015) and sub-grid scale turbulent processes are represented with a 3D Smagorinsky-type turbulence scheme (Halliwell, 2015; Stratton et al., 2015). The cloud microphysics are represented with the Cloud-AeroSol Interacting Microphysics (CASIM) module (see section 2.4). As we are particularly interested in the impact of ice nucleating particles (INPs) in the cloud we conduct sensitivity experiments with different heterogeneous ice nucleation parameterisations as well as different assumptions regarding the incorporation of ice nucleating particles (INP) into cloud droplets, which is pre-requisite for immersion freezing. The details of these sensitivity experiments are described in section 2.4.



2.3 The KiD Model

For the analysis of a large set of wave clouds we conduct additional idealised simulations with the Kinematic Driver Model (KiD, Shipway and Hill (2012); Hill et al. (2015)). The KiD model uses prescribed dynamics to drive different microphysics modules and hence testing of different cloud microphysics and flow configurations in a relatively simple framework. Here, we conduct two-dimensional simulations of wave clouds with different horizontal wavelength (period T between 100s and 1800s), cloud top temperature (t_{ct} between -12°C and -50°C) as well as with different cloud thickness ($z_c = z_{ct} - z_{cb}$ between 1000m and 4000m). This results in a total of 2268 simulations with different flow and/or thermodynamic conditions. All simulations are carried out with a vertical resolution of 50m, 200 vertical levels and a time-step of 1s. At each model level a vertical velocity time series is prescribed:

$$w(t, z) = A \cdot T^{-1} \sin(2\pi t \cdot T^{-1}) \quad (1)$$

with $A = 2880\text{m}$. Multiple simulations are carried out with $T \in [100, 1800]$ s. This formulation leads to a maximum vertical displacement of $\eta = A\pi^{-1} \approx 916.7\text{m}$ irrespective of the chosen period T . The vertical velocity is set to zero after T . The upstream temperature profiles is given by a lapse rate of $-8.104 \cdot 10^{-3} \text{K m}^{-1}$ and a surface temperature of 32.1 K. The initial pressure profile is computed using the hydrostatic approximation with a pressure of 886.2 hPa at 1000m altitude (lowermost level). An initial profile of relative humidity is used with a relative humidity of 45 % below the moist layer, 70 % in the moist layer and a linearly decreasing relative humidity above the moist layer with smooth transitions between the different layers:

$$\text{rh} = \begin{cases} 0.45, & \text{if } z < z_{cb} \\ 0.45 + 0.15 \cos\left(0.5 \cdot \frac{z_{cb,t} - z}{z_{cb,t} - z_{cb}} \cdot \pi\right)^2, & \text{if } z_{cb} \leq z < z_{cb} + 500 \text{ m} \\ 0.7, & \text{if } z_{cb,t} \leq z < z_{ct,t} \\ 0.35 + 0.25 \cos\left(0.5 \cdot \frac{z_{ct,t} - z}{z_{ct,t} - z_{ct,t}} \cdot \pi\right)^2, & \text{if } z_{ct} - 500 \text{ m} \leq z < z_{ct} \\ 0.35 - 4 \cdot 10^{-5}(z - z_{ct}), & \text{if } z \leq z_{ct} \end{cases} \quad (2)$$

The initial profiles are based on the ICE-L case. However, we omit the vertical tilt of the orographic wave as well as the vertical gradient in maximum vertical velocity. Example cross-sections from the KiD simulations are shown in Fig. 9. Cloud microphysics are described by the CASIM module (section 2.4) as in the UM simulations. As in the UM simulations, the sensitivity to the heterogeneous freezing parameterisations as well as assumptions for the CCN activation of INP is tested as detailed in section 2.4. Together with the different settings for dynamic and thermodynamic conditions, we have a total of 45360 two-dimensional, idealised simulations.

2.4 The CASIM module

The Cloud-AeroSol Interacting Microphysics (CASIM) module is a recently developed double-moment cloud microphysics scheme for the UM (Shipway and Hill, 2012; Hill et al., 2015; Stevens et al., 2018; Miltenberger et al., 2018). Hydrometeors



are represented by five different species, the size distribution of which is assumed to be a generalised gamma distribution with a fixed width. Hydrometeor mass and number of each hydrometeor species are computed prognostically. CASIM also includes prognostic mass and number of three soluble and one insoluble aerosol modes, for which log-normal distribution with a fixed width are assumed. Additional tracers for aerosols incorporated into hydrometeors are available, which are transported in accordance with the hydrometeors, i.e. including sedimentation. The in-cloud aerosol tracers allow for an explicit representation of immersion freezing and to investigate the vertical transport of aerosol by hydrometeor sedimentation.

Key microphysical processes to be investigated in the mixed-phase clouds are activation of aerosols to cloud droplets, heterogeneous freezing, growth (sublimation) of ice crystals by vapour deposition, aggregation of ice crystals, and sedimentation of ice phase hydrometeors. All of these processes are represented in the CASIM module. Activation of aerosol to cloud droplets is described with the parameterisation of Abdul-Razzak and Ghan (2000). For the activation of the “insoluble” aerosol category we assume a soluble fraction on the dust particles, which is prescribed as 0.01 %, 0.1 % and 99 % in three sets of sensitivity simulations. The chemical analysis of measured INP by Pratt et al. (2010) suggest that a substantial soluble fraction on INPs is realistic for the considered case. The activated INP particles are then used to predict the ice crystal number concentration using parameterisations of immersion freezing from DeMott et al. (2010) (DM10), Niemand et al. (2012) (N12), Atkinson et al. (2013) (A13), Tobo et al. (2013) (T13) and DeMott et al. (2015) (DM15). For the A13 parameterisation, we assume that 25 % of the dust surface is feldspar. In addition, we have conducted simulations, in which the insoluble aerosol number concentration is directly used in these parameterisations irrespective of whether it was incorporated into liquid first. The latter is the standard approach in all models, that do not track aerosol in hydrometeors. The two sets of sensitivity experiments results in a total of 20 simulations with different representation of immersion freezing. For the sedimentation of ice phase hydrometeors we use fixed diameter-fallspeed relations.

2.5 Trajectory analysis

Kinematic air mass trajectories are computed to detect changes in specific humidity and aerosol number density due to sedimenting hydrometeors in the wave cloud. Trajectories are calculated with the Lagrangian Analysis Tool (Sprenger and Wernli, 2015), which has been adapted to UM output, from the resolved wind-field at 5 min temporal resolution. For the KiD model, trajectories are calculated analytically based on the prescribed wind field (eq. 1).

3 Comparison of modelled cloud properties to observational data

On the 16th November 2007 a wave cloud forming in the lee of the Medicine Bow National Forest was observed with three subsequent aircraft passes through the cloud at different altitudes. The average temperature of the three flight legs is -25°C (leg 1, $z \approx 6.9$ km, ~ 2040 UTC), -27.5°C (leg 2, $z \approx 7.2$ km, ~ 2100 UTC) and -31°C (leg 3, $z \approx 7.7$ km, ~ 2120 UTC). The cloud had an along-flow extension of about 40 km and a vertical extension of at least 1 km. In the UM simulations a wave cloud of similar extent appears at the same location and roughly the same time (± 20 min). A horizontal cross-section of the modelled cloud at ~ 7.2 km, i.e. the mean altitude of flight leg 2, is shown in Fig. 1 a together with the flight tracks. The



215 modelled vertical cloud structure at 42.05°N is shown in Fig. 1 b together with a projection of the aircraft legs on the plane of
the cross-section. These plots already indicate that modelled cloud location and extent agree well with the observed cloud. In
the remainder of this section we compare the observed and modelled cloud microphysical structure in more detail.

3.1 Thermodynamic conditions

220 The geometry of wave clouds is strongly controlled by the upstream humidity and temperature profile as well as the vertical
velocity field.

Fig. 2 a shows a comparison of the upstream temperature profile. The air temperature in the model is slightly higher than ob-
served at all vertical levels, if evaluated at the time and location of the aircraft observations, with a deviation of about 2K for
flight leg 1 and less than 0.1 K for flight leg 3. The model suggests that the upstream temperature varied by up to 2.5K during
the time window of the observations, i.e. between 2040 UTC and 2120 UTC.

225 The upstream specific humidity is compared in Fig. 2 b. In general the model is somewhat more humid than observed at the
time and location of flight leg 3 with a deviation of about 0.2 g kg^{-1} , but agrees very well with the observed specific humidity
at the other flight legs. The model suggests a quite large variability of the upstream specific humidity (roughly by a factor of 2)
in the time window of the observations with a gradual moistening before 2100UTC and a subsequent drying.

In Fig. 3 the observed vertical velocity along the three flight legs is compared to the modelled vertical velocity. While in the
230 figure we also show the vertical velocity interpolated onto the flight path (dark blue), for the analysis we use hypothetical flight
paths, which are parallel to the mean modelled streamline (grey lines). Hypothetical flight paths have a horizontal spacing of
250 m in zonal direction and run through the centre of the wave clouds, i.e. have a peak vertical velocity larger than 2.5 ms^{-1} .
Using these hypothetical flight paths instead of the actual aircraft track eliminates the impact of slightly different horizontal
wind direction in model simulations and the observed flow. The mean flow is from west to east, i.e. from left to right in these
235 plots, and the cloud forms at the first peak in vertical velocity. The amplitude of the wave in terms of the vertical velocity is well
captured in the model at all three altitudes with maximum deviations of less than 1 ms^{-1} . The width of the positive vertical
velocity peak is slightly larger in the model than in the observations and the peak occurs slightly further east. The secondary
peaks in vertical velocity downstream of the main wave are less well captured, particularly at flight leg 3 (Fig. 3 a).

Overall, modelled flow pattern and thermodynamic conditions agree very well with observations (deviation of air temperature
240 $< 1\text{ K}$, specific humidity $< 0.2\text{ g kg}^{-1}$, vertical velocity $< 1\text{ ms}^{-1}$). Hence the simulation can be used for an in-depth com-
parison of the cloud microphysical structure as well as investigations of the vertical fluxes of water vapour and aerosol. Due
to the small temperature basis in the model, in the following we always compare the aircraft data with the model data 200 m
above the altitude of the flight track. This eliminates the temperature basis (SI Fig. 1) and allows for a better comparison of the
ice nucleation.

245 3.2 Cloud structure

The microphysical data along the various aircraft legs allows for a detailed analysis of the microphysical processes due to the
mainly laminar flow in the wave clouds, albeit not providing a truly Lagrangian perspective. The in-cloud, updraft dominated



region of the flight legs is characterised by a relatively constant air temperature (variations < 0.5 K) and specific humidity (variations < 0.1 g kg⁻¹) (Fig. 4 a-c, SI Fig. 1) in both the model and the observational data. The constant specific humidity
250 reflects water saturated conditions given the observed constant in-cloud temperature. Consistent with the similar temperature in model and observation, the in-cloud specific humidity is very similar in both data-sets. This is partly by design as the measured specific humidity was corrected such that the relative humidity is on average 100% in regions with liquid water content larger than 0.02 g kg⁻¹ (Heymsfield et al., 2011).

The deviations in the spatial distribution and amount of total condensate content between model and observations are larger than
255 in all other variables considered so far (Fig. 4 d-f). In the upstream, updraft dominated cloud section, i.e. west of $\sim -105.1^\circ$ E, the total condensate amount is clearly larger than in the observations. In most model runs as well as in the observational data there is little ice in this part of the cloud (Fig. 5) and hence the total condensate is controlled by the upstream humidity and the total lifting up to the considered point. Given the small deviations in upstream humidity between model and observations, the higher modelled total condensate values are likely due to the somewhat larger vertical velocities, which together with the
260 similar horizontal wavelength result in larger vertical displacements of air parcels than in the observations (Fig. 3). Simulations using the A13 parameterisation have an even higher total condensate amount. In these simulations glaciation occurs very early (Fig. 5), hence the saturation pressure over ice is relevant for the equilibrium condensate amount and not the saturation pressure over water. In the cloudy region further downstream, i.e. downstream of $\sim -105.1^\circ$ E, observations indicate a large increase in condensate amount, despite the prevailing downdraft. In the model, there is a small increase of total condensate in
265 this regions most conspicuous for flight leg 3 (Fig. 4 f), but the values are generally much smaller than in the observations. In the model and observation this increase is accompanied by an increase in the ice crystal number concentration, which at least in the model can be directly linked to the sedimentation of frozen hydrometeors from higher altitudes. The cloud droplet number concentration deviates by less than 20 cm⁻³ between model and observations for all simulations except those using A13, for which cloud droplets are depleted due to very efficient heterogeneous freezing (SI Fig. 2).

The comparison of frozen hydrometeor mass mixing ratios shows that the modelled onset of significant cloud glaciation is
270 roughly consistent with the observations along the two upper flight legs at $\sim -105.1^\circ$ E, but occurs later on the flight leg 1 (model: $\sim -105.13^\circ$ E, observations: $\sim -105.18^\circ$ E; Fig. 5 a-c). The steep increase in the mass mixing ratio on the upper two flight legs (downstream of $\sim -105.1^\circ$ E) is associated with a rapid increase in ice number concentration in the model (Fig. 5 d, e) and occurs in the downdraft region suggesting an input of particles formed at higher levels. In the observations
275 this correlation of ice mass mixing ratio and number concentration exists as well, but is not as clear. While significant cloud glaciation also only occurs in the downdraft region, ice crystal number concentration increases further downstream. In the model the air parcels likely experience larger vertical displacements and hence the impact of homogeneous freezing on the ice crystal population at observed along the flight legs is larger than in the observations, i.e. giving rise to a earlier increase in ice crystal number masking the depositional growth of the existing ice crystal population formed by heterogeneous freezing. The
280 first ice crystals larger than 125 μ m appear in approximately the same location as in the observations at all altitudes, however with much larger concentrations. This suggests a too large droplet mass in the freezing event consistent with the overestimation of liquid condensate. Maximum ice crystal concentrations for most simulations agree with in a factor 2 on the lower two flight



legs, while they are about a factor 10 larger on the flight leg 3 (Fig. 5 d-f). As pointed out earlier, simulations using the A13 parameterisation strongly overestimate the ice crystal number concentration inducing a too early onset of glaciation. Different
285 assumptions on the CCN activation of dust particles (different line styles of the same colour in Fig. 5) have only a small impact on the modelled ice crystal mass and number concentrations, with the largest impact in simulations using the N12 parameterisation and flight leg 3. Even for simulations with N12 the resulting differences are much smaller than the difference to the observed time series and it is not clear whether representing CCN activation of dust particles yields an improvement based on this data. As expected the location, at which ice crystals first appear, is shifting slightly downstream in simulations with a
290 smaller soluble fraction on the dust particles. The horizontal extent of the ice tail in the model is overestimated for all flight legs, except flight leg 1 (Fig. 5c, f). The longevity of ice crystal in the model is very likely related to the smaller average ice crystal mass and the untuned parameters used to compute the mean fallspeed from the ice crystal diameter.

In summary, observations and model simulations (except those using the A13 parameterisation) agree on the overall micro-physical structure of the cloud with ice particles and cloud droplets co-existing, a similar location for the appearance of first
295 ice crystals and ice crystals from the homogeneous freezing zone affecting cloud properties in the downdraft region. Despite the overall good agreement, modelled and observed total condensate amount as well as ice crystal number concentration deviate clearly. The former is most likely caused by an overestimation of parcel vertical displacement in the model, while the overestimation in initial ice crystal number is either related to the heterogeneous freezing parameterisations used or a too large diameter of the newly formed ice crystals. In the following section we investigate in more detail how different heterogeneous
300 freezing parameterisations influence the spatial distribution of ice crystal number concentration.

3.3 Temperature dependency of heterogeneous ice formation

The main difference between the various heterogeneous freezing parameterisations is the temperature dependency of INP and the prefactors specifying the INP fraction of dust particles, as illustrated in Fig. 6. While observing the impact of INP temperature dependence in most clouds is challenging due to impacts of sedimentation and strong vertical motion, the laminar flow
305 and quasi-Lagrangian nature of aircraft observations in orographic clouds may facilitate observations if the signature of INP temperature dependence in ice crystal number concentrations. In order to test this hypothesis in the model we compare the ice crystal number concentrations in the updraft region of the cloud with the ice crystal number concentration expected from the heterogeneous freezing parameterisation based on the temperature and the upstream dust profile (compare coloured markers and lines in Fig. 6): In general these agree very well suggesting that we can use observations of ice crystal number concentration from the updraft region of orographic wave clouds to constrain the temperature dependence of INP concentration. The
310 observational data from the ICE-L flight are shown in the black box-plots in Fig. 6 separately for each flight leg. This data suggest a very weak temperature dependency of heterogeneous freezing in the observed wave cloud, which is only consistent with the DM10 parameterisation. All other parameterisations appear to have a too strong temperature dependence. However, the temporal evolution of the upstream dust concentrations has to be considered as this can result in shallower or steeper temperature apparent temperature dependence. As the upstream dust profile was not monitored continuously and is constructed from the upstream observations along the flight legs, only the potential impact of time-varying dust concentrations can be



assessed. For this we use the minimum and maximum observed upstream dust concentrations, irrespective of the observed altitude, to derive the resulting impact on the expected ice crystal number concentration: The shaded area in Fig. 6 indicates the spread in expected number concentrations, while the dashed lines represent a scenario with continuously decreasing upstream dust concentrations. If the latter scenario is considered, the observations are consistent also with the T13 simulation. Reliable observational data of the ice crystal size distribution is only available for particles larger than $125 \mu\text{m}$. Hence, the analysis here considers only the largest observed ice crystal number concentration in the updraft region, which limits the impact of different mean droplet volumes during freezing and potential differences in depositional growth, but introduces additional uncertainty into the comparison.

The comparison shows that all heterogeneous freezing parameterisation, except that from Atkinson et al. (2013) are compatible with the observations within the anticipated uncertainty range. For simulations with the A13 parameterisation we assume feldspar to be constitute 25% of the dust surface, which is at the upper end of the composition of natural dust Atkinson et al. (2013). If a value closer to the lower bound of 1% would have been used, A13 would be closer to the other parameterisations at -25°C but still predicts too high ice crystal concentrations at colder temperatures (SI Fig. 3). The best agreement is obtained for the parameterisations from DeMott et al. (2010) and Tobo et al. (2013). However, it is unclear whether these parameterisations are most applicable in other cases or other geographic regions, as the INP activity is known to strongly depend on the chemical composition and size distribution of aerosols (e.g. Petters and Wright, 2015). Nevertheless, the presented results suggest that wave clouds can be used as natural laboratories to investigate the temperature dependence of heterogeneous freezing. To formulate constraints on the parameterisations observations from more wave cloud events are necessary. In any future campaigns targeting orographic wave clouds, an emphasis should be placed on characterising the full ice crystal size distribution as well as the temporal (and spatial) variation of the upstream aerosol concentration.

4 Modification of water vapour and aerosol profiles

4.1 ICE-L case

One important impact of wave clouds on the evolution of the larger-scale atmospheric state is modification of water vapour and aerosol profiles through sedimentation of hydrometeors (in addition to the alteration of radiative fluxes). Vertical transport of water vapour and aerosols occurs in all clouds, but it is likely easier to observe these fluxes in wave clouds. Here, we quantify the downward transport of water and aerosol by considering the change in total water or aerosol number concentrations along trajectories through the wave cloud. Fig. 7 a and b show the Lagrangian change in total water along backwards trajectories starting in the lee of the cloud for simulations with the A13 and DM10 heterogeneous freezing parameterisations. In the time period after 80 min a typical sedimentation signal is obtained with a depletion of the total water content in parcels above about 7 km and an increase in parcels below. At earlier times, this pattern is repeated twice in the vertical and a closer inspect reveals that there are two cloudy layers in the UM simulations, one formed by homogeneous nucleation and the lower one by heterogeneous freezing. To assess the differences between simulations with different heterogeneous freezing, average profiles for the



350 two time periods from all simulations are shown in Fig. 7 c and d. The shading indicates the variability resulting from different starting latitudes of the trajectories. The mean profiles for simulations with all parameterisations except A13 are very similar and much smaller than the temporal variability. The larger INP concentrations predicted by A13 lead to much larger downward fluxes particularly in the first part of the considered time period. The assumptions on the CCN activation of dust lead to very small differences in the sedimentation flux (SI Fig. 4 a, b).

355 The CASIM microphysics explicitly considers the vertical transport of dust particles by hydrometeor sedimentation and therefore allows us to quantify the downward transport of aerosol by the wave cloud. The Lagrangian change of aerosol content is shown in Fig. 8. The vertical structure is different to the moisture flux, with aerosol depletion only occurring at the very top of the cloud (above ~ 9.7 km) and increases in aerosol number concentrations mainly towards cloud base. The profiles of the vertical dust transport are more sensitive to changes in the heterogeneous freezing parameterisation than the moisture flux,
360 with larger changes also in the shape of the profiles. However, the differences are again smaller than the temporal variability. The treatment of the CCN activation of dust (using all dust for heterogeneous freezing or presenting activation assuming some soluble fraction on dust particles) has a much larger impact on the vertical aerosol transport than on the moisture flux. The resulting differences in the profile are on the same order of magnitude as the temporal variability (SI Fig. 4 c, d).

It would be interesting to constrain these downward fluxes with observational data, in particular given the uncertainties surrounding diameter-fallspeed relations often used in bulk models. The peak downward flux of about 0.1 g kg^{-1} is, however,
365 smaller than the temporal variation of the specific humidity (Fig. 2) during the average time a parcel needs to transit through the wave cloud (i.e. ~ 30 min). As the aircraft data does not provide information on the temporal evolution of upstream humidity, it is not possible to use the aircraft data to constrain the vertical moisture flux. In addition, for such an assessment the construction of air parcel trajectories from the observed velocity field would be required. While this is in principle possible
370 (e.g. Field et al., 2012), for the assessment of sedimentation fluxes the error in the upstream positions of air parcels would need to be smaller than 500 m owing to the vertical gradient of upstream specific humidity. This is not feasible given the sparse observations of velocity (only sampled along flight legs) and the uncertainty in measured vertical velocity. However, detailed observations of the 3D velocity field for example with an on-board Lidar system and a better characterisation of the upstream and downstream humidity profiles, e.g. sampling in a quasi-Lagrangian manner, there is a potential for future field campaigns
375 to constrain vertical sedimentation fluxes from wave clouds.

Because wave clouds offer such an opportunity to detect sedimentation mediated fluxes of moisture and aerosol we assess in the following section how the amplitude of the sedimentation fluxes depend on the upstream thermodynamic conditions, which determine the cloud thickness and cloud top temperature, and on the horizontal wavelength of the gravity wave, that controls the horizontal extent of the cloud.

380 4.2 Downward moisture flux in idealised simulations

The modification of moisture and aerosol profiles by hydrometeor sedimentation is investigated for the ICE-L case study in the previous section. However, the cloud-integrated sedimentation fluxes will vary for different wavelength, cloud top temperatures and cloud thicknesses and so will their impact on the vertical profiles of aerosol and moisture. To assess these dependencies,



we use two-dimensional, idealised simulations with the KiD-model (section 2.3). Using an idealised model for this assessment
385 allows us to vary the wavelength of the gravity wave, which would require changing the topography in the Unified Model.
In addition, we can carry out a large number of simulations sampling a large proportion of the relevant phase-space, which
would not be possible with the UM due to the much larger computational costs. But we are able to link back to the case study
by including the observed case in the phase space explored. Two exemplary realisations of wave cloud in the KiD-model are
shown in Fig. 9 along with the profiles of Lagrangian changes in moisture ($\Delta_{\text{Lagr}q_t}$) and aerosol $\Delta_{\text{Lagr}m_{\text{du}}}$. As in the UM
390 simulations, the profiles of moisture and aerosol changes have distinctly different shapes: While aerosol changes are concentrated
at cloud top and cloud base, moisture changes occurring throughout the cloud with peak values in the upper and lower
half of the cloud, respectively.

To explore the variation of the downward transport as a function of cloud geometry, we focus on the cloud-scale downward
moisture (aerosol) flux Δq_t (Δm_{du}), which we define as the integral of positive $\Delta_{\text{Lagr}q_t}$ ($\Delta_{\text{Lagr}m_{\text{du}}}$). Note that the integral
395 over negative $\Delta_{\text{Lagr}q_t}$ ($\Delta_{\text{Lagr}m_{\text{du}}}$) gives the same results due to mass conservation, albeit of course with a different sign (not
shown). Fig. 10 a summaries Δq_t for all investigated wave periods (abscissa) and cloud top temperatures (ordinate) for a cloud
depth of 2000m. The same metric has been computed from the UM simulations and is shown by the colour-filled circle at
 $T = 1800$ s and $t_{\text{ct}} = -45$ °C, which corresponds to the average cloud top temperature and residence time of parcels in the
orographic cloud for the ICE-L case. In the UM only the central section of the wave-cloud with largest vertical velocities is
400 considered. Δq_t for the three-dimensional UM simulation and the idealised KiD simulation are comparable in value. This
justifies the use of the KiD model to explore the dependence of Δq_t on the upstream thermodynamic profile and the wave
period. In the variation of Δq_t over the sampled part of the phase-space the most prominent feature is the strong increase of
 $\Delta_{\text{Lagr}q_t}$ at about a cloud top temperature of 37 °C, which is due to the onset of homogeneous freezing and hence a large in-
crease in the frozen water content available for sedimentation. For all cloud top temperatures $\Delta_{\text{Lagr}q_t}$ increases towards longer
405 wave periods as expected. Consistent with the UM simulations, the parameterisation used for heterogeneous freezing impacts
the sedimentation fluxes: Fig. 10 b shows the maximum difference between any two simulations with the same wave period,
cloud top temperature and cloud thickness, but different heterogeneous freezing parameterisations. For the UM simulation the
variability is about a factor 5 larger (colour-filled circle in Fig. 10 b), which is mainly due to the low values for the simulation
with DM10 and $\epsilon = 0.01$. The impact of the parameterisation choice is largest for cloud top temperatures just below the onset
410 of homogeneous freezing (see e.g. Fig. 6). In this part of the parameter space $\Delta_{\text{Lagr}q_t}$ varies by up to a factor 10 between
simulations with different heterogeneous freezing parameterisations. Differences between simulations with different heteroge-
neous freezing parameterisations are largest for wave periods larger than 800s and cloud top temperatures between ~ -30 °C
and ~ -38 °C.

The downward transport of aerosol $\Delta_{\text{Lagr}m_{\text{du}}}$ is summarised in Fig. 10 c and d. $\Delta_{\text{Lagr}m_{\text{du}}}$ and its variation with cloud micro-
415 physical parameterisation choices is again very similar to the values obtained from the UM simulation (colour-filled circles in
Fig. 10 c, d). The aerosol downward transport increases, similar to the downward moisture transport, with longer wave periods
and towards colder cloud top temperatures. The increase with decreasing cloud top temperature is, however, smoother than for
 $\Delta_{\text{Lagr}q_t}$. Towards the onset of homogeneous freezing most heterogeneous freezing parameterisations predict that a substantial



fraction of dust is activated as INP and hence there is no step-change at the onset of homogeneous freezing. Differences be-
420 tween simulations with different settings in the cloud microphysics are largest for wave periods larger than 600s and cloud top
temperatures between $\sim -19^\circ\text{C}$ and $\sim -28^\circ\text{C}$.

A conceptual model of the sedimentation fluxes provides insight into the key variables controlling the modification of the
moisture profile and may be used to represent these in models with a lower spatial resolution. Similar to previously pro-
posed conceptual models for orographic precipitation Smith (1979); Smith and Barstad (2004); Seifert and Zängl (2010);
425 Miltenberger et al. (2015), we chose an ansatz based on the consideration of the characteristic timescales of the cloud:

$$\Delta q_t = \left((G_{\text{pot}} - G_{\text{nuc}}) \left(1 - \exp\left(-\frac{\tau_{\text{ic}}}{\tau_{\text{dep}}}\right) \right) + G_{\text{nuc}} \right) \cdot \left(1 - \exp\left(-\frac{\tau_{\text{ic}}}{\tau_{\text{sedi}}}\right) \right) \quad (3)$$

The first term on the left side of the equation describes how much water is transferred from the gas-phase to frozen condensate
due to depositional growth and freezing, while the second term describes the sedimentation of the condensate. Note that we
ignore here the sedimentation of liquid cloud particles, which only has a minor impact compared to the impact of ice crystal
430 sedimentation in the KiD simulations (not shown). The key variables are (i) the potential condensate G_{pot} , which is the maxi-
mum cloud condensate possible given thermodynamic constraints, initial humidity and vertical displacement, (ii) the in-cloud
residence time τ_{ic} , i.e. the time available for cloud microphysical processes, (iii) the timescale for depositional growth of ice
hydrometeors τ_{dep} and (iv) the timescale for sedimentation τ_{sedi} . Note that in contrast to parcel-oriented formulations these
timescales refer to the entire cloud and not to individual air parcels. Finally, G_{nuc} denotes the condensate formed during ice
435 crystal nucleation via homogeneous or heterogeneous freezing. A similar approach has been suggested by Seifert and Zängl
(2010) and Miltenberger et al. (2015) for describing the precipitation formation in warm-phase orographic clouds. As we show
in the following, all parameters in equation 3 can be estimated from the upstream thermodynamic profiles and expected vertical
displacement.

The potential condensate is the maximum condensate amount that would occur along a wave cloud trajectory if the air parcel's
440 ice water content were in thermodynamic equilibrium. In warm-phase clouds the condensate amount in absence of sedimen-
tation is often close to the potential condensate as a result of fairly small vapour deposition timescales (~ 1 s), as e.g. used
in saturation adjustment parameterisations. However, in mixed- and ice-phase clouds the potential condensate is typically not
realised due to the longer timescales for depositional growth (in the order of 1000 s). G_{pot} is not used as a measure of the
condensate formed in the cloud, but as a “virtual” reservoir species from which condensate can be formed. Along air parcel
445 trajectories G_{pot} can be directly computed as the difference between the upstream specific humidity and the saturation pressure
over ice at the coldest point along the trajectory, if latent heating from phase-changes of water are neglected. Using trajectory
data from the KiD experiments, the variation of $G_{\text{pot,Lagr}}$ with the wave period and cloud top temperature can be quantified
(Fig. 11 a). Further G_{pot} can be computed from the wave amplitude A and the upstream temperature t_0 , specific humidity $q_{v,0}$
and pressure p_0 profiles by assuming dry-adiabatic ascent of the parcel (lapse rate γ) and a hydrostatic balanced atmosphere:

$$450 \quad G_{\text{pot}}(z_0) = (q_{v,0} - q_{i,\text{sat}}(t_0 + A\gamma)) p_{z_0+A} \quad (4)$$

Integrating above equation over all altitudes where $q_{v,0} > q_{i,\text{sat}}(t + A\gamma)$ gives an estimate of G_{pot} , which for our KiD simu-
lations deviates less than 5% from the Lagrangian estimate shown in Fig. 11 a (SI Fig. 5 a).



Another important cloud microphysical variable, that will be required for parameterising the characteristic timescales is the number of ice crystals in each cloud. To characterise the variability across the different clouds, we use only the maximum possible number of ice crystals $n_{i, \max}$ formed either by homogeneous or heterogeneous freezing. In the Lagrangian data, this is the integral of homogeneous and heterogeneous nucleation rates along the trajectory passing just below cloud top. Fig. 11 b shows that $n_{i, \max, \text{Lagr}}$ depends strongly on cloud top temperature with a major increase around $t_{\text{ct}} \approx -38^\circ\text{C}$ reflecting the transition to clouds dominated by homogeneous freezing. For clouds with colder cloud tops there is also a clear dependence on the time period of the wave clouds reflecting the interaction between the nucleation and growth of newly formed ice crystals (e.g. Kärcher et al., 2006). For the conceptual model, we find that using the heterogeneous parameterisation used in the KiD model together with the minimum temperature expected from the maximum vertical displacement gives a reasonable estimate for temperatures warmer than -38°C . For colder cloud-top temperatures, we use the homogeneous nucleation rate from the DM10 parameterisation (consistent with CASIM microphysics) and a correction factor depending on the wave period: $0.932 \cdot \log_{10}(T) + 0.228$ for $t_{\text{ct}} < -42.5^\circ\text{C}$ and $1.48 \cdot \log_{10}(T) - 1.48$ for $t_{\text{ct}} > -42.5^\circ\text{C}$. Closely related to the ice crystal number is also the term G_{nuc} describing the ice crystal mass formed by homogeneous or heterogeneous freezing. G_{nuc} can be estimated from $n_{i, \max}$ and a typical particle mass \bar{q}_i , which can be directly obtain from the KiD simulations: $\bar{q}_i = 10^{-11.5} \text{ kg kg}^{-1}$ ($10^{-9.6} \text{ kg kg}^{-1}$) for clouds dominated by homogeneous (heterogeneous) freezing. The in-cloud residence time τ_{ic} describes the time available for condensate and precipitation formation (e.g. for warm clouds Miltenberger et al., 2015). Here, we define τ_{ic} as time during which air parcels are super-saturated with respect to ice. This timescale $\tau_{\text{ic, Lagr}}$ can be directly quantified from the KiD-model air mass trajectories (Fig. 12 a) or analytically calculated from the prescribed wave flow and the upstream humidity profile:

$$\tau_{\text{ic}} = T \cdot (1 - \arccos(1 - 0.5 \cdot \eta_{i, \text{sat}} A \pi^{-1}) \pi^{-1}) \quad (5)$$

with $\eta_{i, \text{sat}}$ the vertical displacement required to reach ice saturation). The deviations between this estimate and the Lagrangian metric are less than 5 % (SI Fig. 5 b). From the resulting vertical profile of τ_{ic} the largest timescale is selected (only considering cloudy parcels).

The depositional timescale τ_{dep} describes the characteristic timescale for the reduction of ice supersaturation for $w = 0 \text{ m s}^{-1}$ and an ice crystal population characterised by the number concentration n_i and mean ice particle diameter d_i . The concept of describing depositional growth of ice crystals with a characteristic timescale τ_{dep} is frequently used in literature and cloud microphysical parameterisations (e.g. Khvorostyanov, 1995): $\tau_{\text{dep}} = (g n_i d_i c_i f)^{-1}$, where $g = 4 \cdot (L_{\text{ed}}^2 (K_t R_d t^2)^{-1} + R_d t (D_{\text{vtp}} e_{s, i})^{-1})^{-1}$, c_i the capacitance of the ice crystals, and f a ventilation factor. This concept needs to be extended to a single characteristic timescale for the entire cloud. To estimate this timescale we again utilise the KiD simulations. The cloud-scale deposition timescale can be estimated from the integrated deposition D and freezing rates G_{nuc} as well as τ_{ic} according to: $\tau_{\text{dep, Lagr}} = \tau_{\text{ic, Lagr}} (\log(1 - D(G_{\text{pot}} - G_{\text{nuc}})^{-1})^{-1})^{-1}$. The resulting estimates are shown in Fig. 12 b. Immediately obvious is an inverse relation to the ice crystal number concentration, as expected from air parcel considerations, but this is not the sole determinant. In order to estimate τ_{dep} from the a-priori known parameters, i.e. upstream profiles and vertical displacement, we



determined the following least-square fits to the KiD model data (SI Fig. 5 c):

$$\tau_{\text{dep}} = \begin{cases} 5.29 \cdot 10^{10} \cdot n_i^{-1.94} \cdot T^{-0.558} \cdot z_c^{0.539}, & \text{if } t_{\text{ct}} \geq -34.25 \text{ K} \\ 1.71 \cdot 10^7 \cdot n_i^{-0.764} \cdot T^{-0.716} \cdot z_c^{0.696} \cdot (n_i T)^{0.0566}, & \text{if } -44.3 \text{ K} < t_{\text{ct}} < -34.25 \text{ K} \\ 1.34 \cdot 10^7 \cdot n_i^{-0.749} \cdot T^{-0.271} \cdot z_c^{0.576}, & \text{if } t_{\text{ct}} \leq -44.3 \text{ K} \end{cases} \quad (6)$$

The sub-division is necessary due to the fundamentally different behaviour in the parts of the parameter space dominated by homogeneous and heterogeneous freezing, respectively.

490 Finally, the sedimentation timescale needs to be determined, for which we use the same approach as for the deposition timescale, i.e. diagnosing a cloud-wide timescale from the KiD model and constructing a statistical model. The timescale is estimated from the KiD model according to: $\tau_{\text{sedi,L}} = \tau_{\text{ic,L}} (\log(1 - \Delta q_{\text{sedi}}(D + G_{\text{nuc}})^{-1}))^{-1}$. The results are shown in Fig. 12 c. The sedimentation velocity in the KiD model is described using a pre-scribed diameter-fallspeed relation. Consistently, the τ_{sedi} increases for clouds with larger n_i . In addition to this information, we find that it is necessary to incorporate
 495 information on the time period and cloud thickness in the statistical model likely due to their impact on the cloud microphysical evolution (SI Fig. 5 d):

$$\tau_{\text{sedi}} = \begin{cases} 4.01 \cdot 10^3 \cdot n_i^{-0.0185 \cdot T - 0.242 z_c - 0.449} \cdot T^{0.0253 t_{\text{ct}} - 0.467}, & \text{if } t_{\text{ct}} \geq -32.2 \text{ K} \\ 4.26 \cdot 10^4 \cdot n_i^{-0.0507 \cdot T - 0.326 z_c + 1.03} \cdot T^{0.663 t_{\text{ct}} - 2.43}, & \text{if } -38.5 \text{ K} < z_{\text{ct}} < -32.2 \text{ K} \\ 3.06 \cdot 10^4 \cdot n_i^{0.385 \cdot T - 0.0613 z_c - 0.500} \cdot T^{-0.143 t_{\text{ct}} - 1.65}, & \text{if } z_{\text{ct}} \leq -38.5 \text{ km} \end{cases} \quad (7)$$

By using equations 3 to 7 with the described approximation of $n_{i,\text{max}}$ the cloud-scale sedimentation flux can be computed based on the upstream dust concentration, the upstream profiles of temperature, humidity and pressure and the maximum
 500 vertical displacement. The parameterised sedimentation flux is shown in Fig. 13 a. Comparing this figure with the results from the full KiD model (Fig. 10 a) shows very similar dependencies on wave period and cloud-top temperature. Note that Fig. 10 a shows the average sedimentation flux from simulations with different heterogeneous freezing parameterisation, while Fig. 13 a shows data only for simulations with DM10. Hence the differences in absolute values. The absolute values from the conceptual model agree well with the simulations from the full KiD model with discrepancies mostly smaller than 30 % (Fig. 13).

505 5 Conclusions

Orographic wave clouds impact atmospheric flow by interacting with radiative fluxes and by modifying the moisture and aerosol profiles. Furthermore due to the laminar flow they are ideal natural laboratories to explore cloud microphysical processes. Here, we compare simulations with the Unified Model (UM) including the recently developed Cloud-Aerosol Interacting Microphysics (CASIM) module to observations from the ICE-L measurement campaign, which took place in 2007 over
 510 the central US.

High-resolution simulations with the UM capture the thermodynamic structure and vertical velocity field very well with deviations of less than 1 K for air temperature, 0.2 g kg⁻¹ for specific humidity and 1 ms for vertical velocity. The overall cloud



microphysical structure of the cloud is similar to the observations, although there are significant difference in the impact of homogeneous freezing, the extend of ice tail of the cloud and the size distribution. Some of the differences could be explained
515 by an overestimation of the vertical displacement in the model, but problems with the cloud microphysical parameterisation can also not be excluded. More detailed information on the 3D wind field would be helpful for future studies. Several heterogeneous freezing parameterisations have been proposed in recent years and we explicitly tested their impact on the cloud structure. Most tested heterogeneous freezing parameterisations gave very similar results. The main difference between simulations with the different schemes is the vertical gradient of ice crystal number concentration in the updraft region of the cloud, all
520 other investigated cloud properties display only a very small sensitivity. For all tested parameterisations, except Atkinson et al. (2013), the vertical gradient of the ice crystal number concentration is consistent with the observations given the uncertainty in observations and their representativity. The best agreement is obtained for simulations with DeMott et al. (2010). As CASIM explicitly models dust particles in liquid and ice hydrometeors, we also tested the impact of using also dust incorporated in liquid droplets for heterogeneous freezing and of prescribing different soluble fractions on dust aerosols. Both made only very
525 little impact on the cloud microphysical structure. Despite the well captured thermodynamic conditions and flow dynamics, vigorous conclusion about link between ice crystal number concentration and upstream aerosol, in particular the temperature dependence of heterogeneous freezing, are difficult to arrive at. For this purpose, future campaigns need to provide a better characterisation of the upstream profiles of aerosols and their temporal evolution as well as observations of the full ice crystal size distribution (here limited to particles larger than $125 \mu\text{m}$). The advance in measurement techniques over the past years
530 allows to meet these requirements in future field campaigns.

The simulations were further used to investigate the modification of moisture and aerosol profiles by the sedimentation of hydrometeors in the wave cloud. The latter was only possible due to the novel capabilities of the CASIM module. Lagrangian estimates suggest a different vertical structure of the aerosol and moisture changes, with those for aerosols concentrated at cloud top and cloud base. However, the fairly small changes in the profiles ($< 0.1 \text{ g kg}^{-1}$ for moisture, $< 0.1 \text{ cm}^{-3}$ for aerosol) pre-
535 vent to constrain the sedimentation fluxes with observations.

Two-dimensional, idealised simulations were developed to further investigate the parameter space, with a particular focus on the dependence of the moisture and aerosol sedimentation fluxes on the cloud geometry, i.e. the wavelength, cloud top temperature and cloud thickness. The sensitivity to the heterogeneous freezing parameterisation is found to be largest for wave periods larger than 1000s and cloud top temperatures between -30 K and -40 K . The modifications of the moisture and aerosol pro-
540 files are largest for clouds with long wave periods and cloud top temperatures colder than $-40 \text{ }^\circ\text{C}$. The Lagrangian change of water content is on the order of 0.1 g kg and that of dust number concentration on the order of 0.1 cm^{-3} , i.e. comparable to the results obtained for the ICE-L case. Based on the idealised KiD simulations we develop a conceptual model that depends on the potential condensate, in-cloud residence timescale, deposition timescale and sedimentation timescale. Lagrangian estimates of the latter two timescales are used to derive an approximation to the timescales, while the other necessary variables can be
545 calculated analytically from the upstream thermodynamic and aerosol profiles. The resulting model captures the variability of the sedimentation flux in a large part of the phase space with deviations less than 30 % for almost all parameter combinations. The error is somewhat larger for cloud top temperatures between $-36 \text{ }^\circ\text{C}$ and $-42 \text{ }^\circ\text{C}$, i.e. in the transition region between



clouds dominated by heterogeneous and those dominated by homogeneous freezing.

While it is not possible to constrain the downward transport of aerosol or water vapour with the observations available from
550 ICE-L, future aircraft campaigns targeting orographic wave clouds would be useful to quantify these important processes and
provide constraints on aerosol transport processes also for more comprehensive aerosol models such as UK Chemistry and
Aerosol Model (UKCA, e.g. Planche et al., 2017). Any future campaign should aim at a better characterisation of the the
upstream and downstream moisture and aerosol profiles including their temporal evolution and a characterisation of the 3D
velocity field. The idealised simulations show that clouds with wave periods larger than 1000s and cloud top temperatures
555 between $\sim -19^\circ\text{C}$ and $\sim -28^\circ\text{C}$ ($\sim -30^\circ\text{C}$ and $\sim -38^\circ\text{C}$) show a large sensitivity of the downward aerosol (humid-
ity) transport to choices in the cloud microphysical parametrisation. Similarly, differences between simulations with different
heterogeneous freezing parameterisations are largest for wave periods larger than 800s and cloud top temperatures between
 $\sim -30^\circ\text{C}$ and $\sim -38^\circ\text{C}$. These regions of the phase space therefore would be interesting to target in future observational
campaigns.

560 *Code availability.* The source code of the KiD-A model version used here and the namelist files are archived in a private directory on
bitbucket.org (amiltenberger/kida_model_with_taubin_casim_icel). Access will be granted by the authors on re-
quest.

Data availability. Model data is stored on the tape archive provided by JASMIN (<http://www.jasmin.ac.uk/>) service and can be provided by
the author on request.

565 *Author contributions.* All authors contributed to the development of the concepts and ideas presented in this paper. A. A. Hill developed the
KiD model. A. K. Miltenberger developed the model set-up with major contributions from P. R. Field for the UM simulations and A. A. Hill
for the KiD set-up. P. R. Field provided expertise on the observational data. All model simulations and the subsequent data analysis were
performed by A. K. Miltenberger. She also wrote the majority of the manuscript with input and comments from all co-authors.

Competing interests. The authors declare that they have no conflict of interest.

570 *Acknowledgements.* We thank Ben Shipway and Jonathan Wilkinson for designing CASIM and incorporating it into the UM model. A. Mil-
tenberger also thanks Axel Seifert for insightful discussions on the characteristic timescales of ice-phase orographic clouds. We acknowledge
the efforts of the ICE-L team for obtaining the observational data. Further, we acknowledge use of the Monsoon2 system, a collaborative
facility supplied under the Joint Weather and Climate Research Programme, a strategic partnership between the Met Office and the Natural

<https://doi.org/10.5194/acp-2019-940>
Preprint. Discussion started: 20 January 2020
© Author(s) 2020. CC BY 4.0 License.



Environment Research Council. All KiD simulations and data analysis were performed on JASMIN, the UK's collaborative data analysis
575 environment (<http://jasmin.ac.uk>).



References

- Abdul-Razzak, H. and Ghan, S. J.: A parameterization of aerosol activation. 2. Multiple aerosol types, *J. Geophys. Res.*, 105, 6837–6844, 2000.
- Aranami, K., Zerroukat, M., and Wood, N.: Mixing properties of SLICE and other mass-conservative semi-Lagrangian schemes, *Q. J. R. Meteorol. Soc.*, 140, 2084–2089, <https://doi.org/10.1002/qj.2268>, 2014.
- 580 Aranami, K., Davies, T., and Wood, N.: A mass restoration scheme for limited-area models with semi-Lagrangian advection, *Q. J. R. Meteorol. Soc.*, 141, 1795–1803, <https://doi.org/10.1002/qj.2482>, 2015.
- Atkinson, J. D., Murray, B. J., Woodhouse, M. T., Whale, T. F., Baustian, K. J., Carslaw, K. S., Dobbie, S., O’Sullivan, D., and Malkin, T. L.: The importance of feldspar for ice nucleation by mineral dust in mixed-phase clouds, *Nature*, 498, 355–358, 585 <https://doi.org/doi:10.1038/nature12278>, 2013.
- Baker, B. A. and Lawson, R. P.: In Situ Observations of the Microphysical Properties of Wave, Cirrus, and Anvil Clouds. Part I: Wave Clouds, *J. Atmos. Sci.*, 63, 3160–3185, <https://doi.org/10.1175/JAS3802.1>, 2006.
- Bergeron, T.: On the physics of cloud and precipitation, *Mémoire présenté à l’Association de Météorologie de l’U.G.G.I. Lissabon Septembre 1933*. Paris Imprimerie Paul Dupont, 1935.
- 590 Clark, P., Roberts, N., Lean, H., Ballard, S. P., and Charlton-Perez, C.: Convection-permitting models: a step-change in rainfall forecasting, *Meteorol. Appl.*, 23, 165–181, <https://doi.org/10.1002/met.1538>, mET-14-0154.R1, 2016.
- Colle, B. A. and Zeng, Y.: Bulk microphysical sensitivities within the MM5 for orographic precipitation. Part I: The Sierra 1986 event, *Mon. Wea. Rev.*, 132, 2780–2801, 2004.
- Cotton, R. J. and Field, P. R.: Ice nucleation characteristics of an isolated wave cloud, *Q. J. R. Meteorol. Soc.*, 128, 2417–2437, 595 <https://doi.org/10.1256/qj.01.150>, 2002.
- Dearden, C., Connolly, P. J., Choulaton, T., Field, P. R., and Heymsfield, A. J.: Factors influencing ice formation and growth in simulations of a mixed-phase wave cloud, *J. Adv. Model. Earth Systems*, 4, <https://doi.org/10.1029/2012MS000163>, 2012.
- DeMott, P. J., Prenni, A. J., Liu, X., Kreidenweis, S. M., Petters, M. D., Twohy, C. H., Richardson, M. S., Eidhammer, T., and Rogers, D. C.: Predicting global atmospheric ice nuclei distributions and their impacts on climate, *Proc. Natl. Acad. Sci. USA*, 107, 11 217–11 222, 600 <https://doi.org/10.1073/pnas.0910818107>, 2010.
- DeMott, P. J., Prenni, A. J., McMeeking, G. R., Sullivan, R. C., Petters, M. D., Tobo, Y., Niemand, M., Möhler, O., Snider, J. R., Wang, Z., and Kreidenweis, S. M.: Integrating laboratory and field data to quantify the immersion freezing ice nucleation activity of mineral dust particles, *Atmos. Chem. Phys.*, 15, 393–409, <https://doi.org/10.5194/acp-15-393-2015>, 2015.
- Eidhammer, T., DeMott, P. J., Prenni, A. J., Petters, M. D., Twohy, C. H., Rogers, D. C., Stith, J., Heymsfield, A., Wang, Z., Pratt, K. A., 605 Prather, K. A., Murphy, S. M., Seinfeld, J. H., Subramanian, R., and Kreidenweis, S. M.: Ice Initiation by Aerosol Particles: Measured and Predicted Ice Nuclei Concentrations versus Measured Ice Crystal Concentrations in an Orographic Wave Cloud, *J. Atmos. Sci.*, 67, 2417–2436, <https://doi.org/10.1175/2010JAS3266.1>, 2010.
- Field, P. R., Cotton, R. J., Johnson, D., Noone, K., Glantz, P., Kaye, P. H., Hirst, E., Greenaway, R. S., Jost, C., Gabriel, R., Reiner, T., Andreae, M., Saunders, C. P. R., Archer, A., Choulaton, T., Smith, M., Brooks, B., Hoell, C., Bandy, B., and Heymsfield, 610 A.: Ice nucleation in orographic wave clouds: Measurements made during INTACC, *Q. J. R. Meteorol. Soc.*, 127, 1493–1512, <https://doi.org/10.1002/qj.49712757502>, 2001.



- Field, P. R., Heymsfield, A. J., Shipway, B. J., DeMott, P. J., Pratt, K. A., Rogers, D. C., Stith, J., and Prather, K. A.: Ice in clouds experiment-layer clouds. Part II: Testing characteristics of heterogeneous ice formation in lee wave clouds, *J. Atmos. Sci.*, 69, 1066–1079, 2012.
- Findeisen, W.: Die kolloidmeteorologischen Vorgänge bei der Niederschlagsbildung (Colloidal meteorological processes in the formation of precipitation), *Meteorol. Zs.*, 55, 121–133, (translated and edited by Volken, E., Giesche, A. M., and S. Brönnimann in *Meteorol. Zs.*, 55, 121–133, 10.1127/metz/2015/0675), 2015.
- 615 Grubisic, V. and Billings, B. J.: Climatology of the Sierra Nevada Mountain-Wave Events, *Mon. Wea. Rev.*, 136, 757–768, <https://doi.org/10.1175-2007MWR1902.1>, 2008.
- Halliwell, C.: Subgrid turbulence scheme, Unified model documentation paper 028, Met Office, 2015.
- 620 Hande, L. B. and Hoose, C.: Partitioning the primary ice formation modes in large eddy simulations of mixed-phase clouds, *Atmos. Chem. Phys.*, 17, 14 105–14 118, <https://doi.org/10.5194/acp-17-14105-2017>, 2017.
- Henneberg, O., Henneberger, J., and Lohmann, U.: Formation and development of orographic mixed-phase clouds, *J. Atmos. Sci.*, 74, 3703–3724, <https://doi.org/10.1175/JAS-D-16-0348.1>, 2017.
- Heymsfield, A. J. and Miloshevich, L. M.: Homogeneous Ice Nucleation and Supercooled Liquid Water in Orographic Wave Clouds, *J. Atmos. Sci.*, 50, 2335–2353, [https://doi.org/10.1175/1520-0469\(1993\)050<2335:HINASL>2.0.CO;2](https://doi.org/10.1175/1520-0469(1993)050<2335:HINASL>2.0.CO;2), 1993.
- 625 Heymsfield, A. J., Field, P. R., Bailey, M., Rogers, D., Stith, J., Twohy, C., Wang, Z., and Haimov, S.: Ice in clouds experiment-layer clouds. Part I: Ice growth rates derived from lenticular wave cloud penetrations, *J. Atmos. Sci.*, 68, 2628–2654, 2011.
- Hill, A. A., Shipway, B. J., and Boutle, I. A.: How sensitive are aerosol-precipitation interactions to the warm rain representation?, *J. Adv. Model. Earth Syst.*, 7, 987–1004, <https://doi.org/10.1002/2014ms000422>, <http://dx.doi.org/10.1002/2014MS000422>, 2015.
- 630 Houze, R. A. J.: Orographic effects on precipitating clouds, *Rev. Geophys.*, 50, RG0001, <https://doi.org/10.1029/2011RG000365>, 2012.
- Jiang, Q. and Smith, R. B.: Cloud Timescales and Orographic Precipitation, *J. Atmos. Sci.*, 60, 1543 – 1559, 2003.
- Johnson, J. S., Cui, Z., Lee, L. A., Gosling, J. P., Blyth, A. M., and Carslaw, K. S.: Evaluating uncertainty in convective cloud microphysics using statistical emulation, *J. Adv. Model. Earth Syst.*, 7, 162–187, <https://doi.org/10.1002/2014MS000383>, 2015.
- Joos, H., Spichtinger, P., Lohmann, U., Gayet, J.-F., and Minikin, A.: Orographic cirrus in the global climate model ECHAM5, *J. Geophys. Res.*, 113, D18 205, 2008.
- 635 Joos, H., Spichtinger, P., Reutter, P., and Fusian, F.: Influence of heterogeneous freezing on the microphysical and radiative properties of orographic cirrus clouds, *Atmos. Chem. Phys.*, 14, 6835–6852, <https://doi.org/10.5194/acp-14-6836-2014>, 2014.
- Kärcher, B., Hendricks, J., and Lohmann, U.: Physically based parameterization of cirrus cloud formation for use in global atmospheric models, *J. Geophys. Res.*, 111, D01 205, <https://doi.org/10.1029/2005JD006219>, 2006.
- 640 Khvorostyanov, V. I.: Mesoscale processes of cloud formation, cloud-radiation interaction, and their modelling with explicit cloud microphysics, *Atmos. Res.*, 39, 1–67, 1995.
- Meyers, M. P., DeMott, P. J., and Cotton, W. R.: New primary ice-nucleation parameterizations in an explicit cloud model, *J. Appl. Meteor.*, 31, 708–721, 1992.
- Miltenberger, A. K., Seifert, A., Joos, H., and Wernli, H.: Scaling relation for warm-phase orographic precipitation - A Lagrangian analysis for 2D mountains, *Q. J. R. Meteorol. Soc.*, 141, 2185–2198, <https://doi.org/10.1002/qj.2514>, 2015.
- 645 Miltenberger, A. K., Field, P., Hill, A., Rosenberg, P., Shipway, B., Wilkinson, J., Scovell, R., and Blyth, A. M.: Aerosol-cloud interactions in mixed-phase convective clouds. Part 1: Aerosol perturbations, *Atmos. Chem. Phys.*, 18, 3119–3145, <https://doi.org/10.5194/acp-18-3119-2018>, 2018.



- Mühlbauer, A. and Lohmann, U.: Sensitivity Studies of Aerosol–Cloud Interactions in Mixed-Phase Orographic Precipitation, *J. Atmos. Sci.*, 66, 2517–2538, <https://doi.org/10.1175/2009JAS3001.1>, 2009.
- Mühlbauer, A., Hashino, T., Xue, L., Teller, A., Lohmann, U., Rasmussen, R. M., Geresdi, I., and Pan, Z.: Intercomparison of aerosol-cloud-precipitation interactions in stratiform orographic mixed-phase clouds, *Atmos. Chem. Phys.*, 10, 8173–8196, <https://doi.org/10.5194/acp-10-8173-2010>, 2010.
- Niemand, M., Möhler, O., Vogel, B., Vogel, H., Hoose, C., Connolly, P., Klein, H., Bingemer, H., DeMott, P., Skrotzki, J., and Leisner, T.: A particle-surface-area-based parameterization of immersion freezing on desert dust particles, *J. Atmos. Sci.*, 69, 3077–3092, <https://doi.org/10.1175/JAS-D-11-0249.1>, 2012.
- Petters, M. D. and Wright, T. P.: Revisiting ice nucleation from precipitation samples, *Geophys. Res. Lett.*, 42, 8758–8766, <https://doi.org/10.1002/2015GL065733>, 2015.
- Planche, C., Mann, G. W., Carslaw, K. S., Dalvi, M., Marsham, J. H., and Field, P. R.: Spatial and temporal CCN variations in convection-permitting aerosol microphysics simulations in an idealised marine tropical domain, *Atmospheric Chemistry and Physics*, 17, 3371–3384, <https://doi.org/10.5194/acp-17-3371-2017>, 2017.
- Pousse-Nottelmann, S., Zubler, E. M., and Lohmann, U.: Microphysical processing of aerosol particles in orographic clouds, *Atmos. Chem. Phys.*, 15, 9217–9236, <https://doi.org/10.5194/acp-15-9217-2015>, 2015.
- Pratt, K. A., Twohy, C. H., Murphy, S. M., Mofet, R. C., Heymsfield, A. J., Gaston, C. J., DeMott, P. J., Field, P. R., Henn, T. R., Rogers, D. C., Gilles, M. K., Seinfeld, J. H., and Prather, K. A.: Observation of playa salts as nuclei in orographic wave clouds, *J. Geophys. Res.*, 115, D15 301, <https://doi.org/10.1029/2009JD013606>, 2010.
- Sawyer, J. S.: The physical and dynamical problems of orographic rain, *Weather*, 11, 375–381, 1956.
- Seifert, A. and Zängl, G.: Scaling relations in warm-rain orographic precipitation, *Meteorol. Z.*, 19, 1–10, <https://doi.org/10.1127/0941-2948/2010/0474>, 2010.
- Shipway, B. J. and Hill, A. A.: Diagnosis of systematic differences between multiple parametrizations of warm rain microphysics using a kinematic framework, *Q. J. R. Meteorol. Soc.*, 138, 2196–2211, <https://doi.org/10.1002/qj.1913>, 2012.
- Smith, R. B.: The influence of mountains on the atmosphere, *Adv. Geosci.*, 21, 87–230, 1979.
- Smith, R. B. and Barstad, I.: A Linear Theory of Orographic Precipitation, *J. Atmos. Sci.*, 61, 1377–1391, 2004.
- Smith, S. A., Field, P. R., Vosper, S. B., Shipway, B. J., and Hill, A. A.: A parameterization of sub-grid orographic rain enhancement via the seeder-feeder effect, *Q. J. R. Meteorol. Soc.*, <https://doi.org/10.1002/qj.2637>, 2015.
- Sprenger, M. and Wernli, H.: The Lagrangian analysis tool LAGRANTO - version 2.0, *Geosci. Model Dev.*, 8, 2569–2586, <https://doi.org/10.5194/gmd-8-2569-2015>, 2015.
- Stevens, R. G., Loewe, K., Dearden, C., Dimitrellos, A., Possner, A., Eirund, G. K., Raatikainen, T., Hill, A. A., Shipway, B. J., Wilkinson, J., Romakkaniemi, S., Tonttila, J., Laaksonen, A., Korhonen, H., Connolly, P., Lohmann, U., Hoose, C., Ekman, A. M. L., Carslaw, K. S., and Field, P. R.: A model intercomparison of CCN-limited tenuous clouds in the high Arctic, *Atmos. Chem. Phys.*, 18, 11 041–11 071, <https://doi.org/10.5194/acp-18-11041-2018>, 2018.
- Stratton, R., Willet, M., Derbyshire, S., Wong, R., and Whitall, M.: Convection Schemes, Unified model documentation paper 027, Met Office, 2015.
- Targino, A. C., Krejci, R., Noone, K. J., and Glantz, P.: Single particle analysis of ice crystal residuals observed in orographic wave clouds over Scandinavia during INTACC experiment, *Atmos. Chem. and Phys.*, 6, 1977–1990, <https://doi.org/10.5194/acp-6-1977-2006>, 2006.



- Tobo, Y., Prenni, A. J., DeMott, P. J., Huffman, J. A., McCluskey, C. S., Tian, G., Pöhlker, C., Pöschl, U., and Kreidenweis, S. M.: Biological aerosol particles as a key determinant of ice nuclei populations in a forest ecosystem, *J. Geophys. Res.*, 118, 10 100–10 110, <https://doi.org/10.1002/jgrd.50801>, 2013.
- 690 Vergara-Temprado, J., Miltenberger, A. K., Furtado, K., Grosvenor, D. P., Shipway, B. J., Hill, A. A., Wilkinson, J. M., Field, P. R., Murray, B. J., and Carslaw, K. S.: Strong control of Southern Ocean cloud reflectivity by ice-nucleating particles, *Proc. Natl. Acad. Sci. USA*, 115, 2687–2692, <https://doi.org/10.1073/pnas.1721627115>, 2018.
- Vosper, S. B., Wells, H., Sinclair, J. A., and Sheridan, P. F.: A climatology of lee waves over the UK derived from model forecasts, *Meteorol. Appl.*, 20, 466–481, <https://doi.org/10.1002/met.1311>, 2013.
- 695 Walters, D., Boutle, I., Brooks, M., Melvin, T., Stratton, R., Vosper, S., Wells, H., Williams, K., Wood, N., Allen, T., Bushell, A., Copsey, D., Earnshaw, P., Edwards, J., Gross, M., Hardiman, S., Harris, C., Heming, J., Klingaman, N., Levine, R., Manners, J., Martin, G., Milton, S., Mittermaier, M., Morcrette, C., Riddick, T., Roberts, M., Sanchez, C., Selwood, P., Stirling, A., Smith, C., Suri, D., Tennant, W., Vidale, P. L., Wilkinson, J., Willett, M., Woolnough, S., and Xavier, P.: The Met Office Unified Model Global Atmosphere 6.0/6.1 and JULES Global Land 6.0/6.1 configurations, *Geosci. Model Dev.*, 10, 1487–1520, <https://doi.org/10.5194/gmd-10-1487-2017>, 2017.
- 700 Xiao, H., Yin, Y., Jin, L., Chen, Q., and Chen, J.: Simulation of the effects of aerosol on mixed-phase orographic clouds using the WRF model with a detailed bin microphysics scheme, *J. Geophys. Res. Atmo.*, 120, 8345–8358, <https://doi.org/10.1002/2014JD022988>, 2015.
- Xue, L., Teller, A., Rasmussen, R., Geresdi, I., Pan, Z., and Liu, X.: Effects of Aerosol Solubility and Regeneration on Mixed-Phase Orographic Clouds and Precipitation, *J. Atmos. Sci.*, 69, 1994–2010, <https://doi.org/10.1175/JAS-D-11-098.1>, 2012.
- Zubler, E. M., Lohmann, U., Lüthi, D., Schär, C., and Muhlbauer, A.: Statistical Analysis of Aerosol Effects on Simulated Mixed-Phase Clouds and Precipitation in the Alps, *J. Atmos. Sci.*, 68, 1474–1492, <https://doi.org/10.1175/2011JAS3632.1>, 2011.

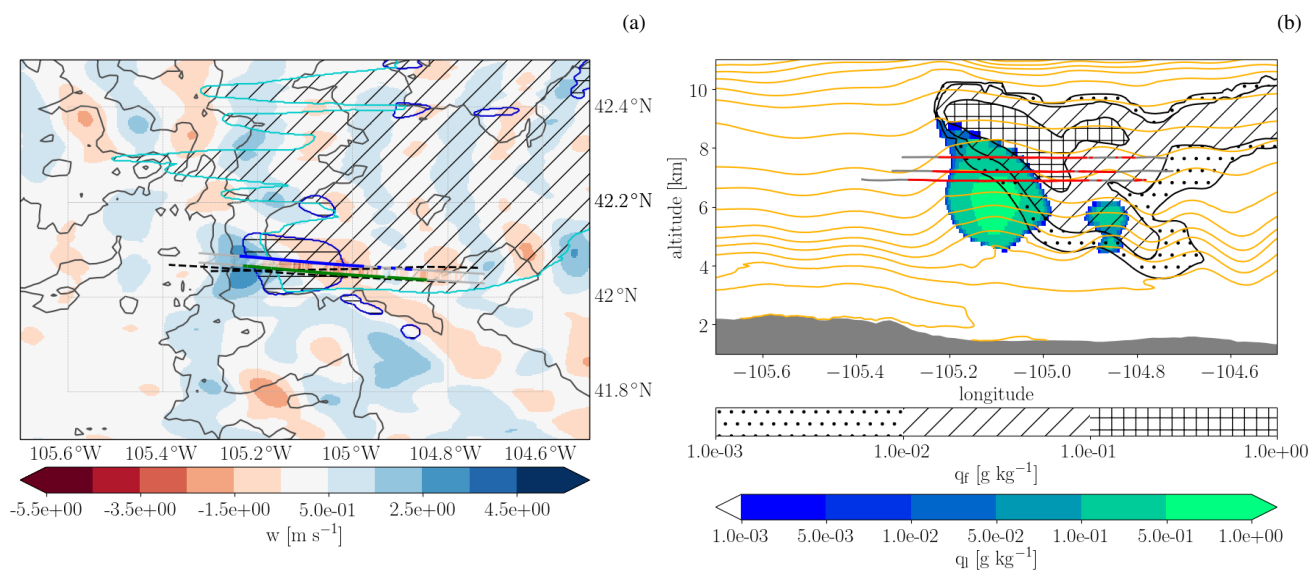


Figure 1. (a) The modelled vertical velocity field at 7200 m, i.e. approximately the altitude of the second aircraft leg, is shown by the colour shading (2100 UTC). The dark blue (cyan) contour and horizontal (diagonal) hatching indicates where liquid (frozen) cloud water content in the model exceeds $10^{-7} \text{ kg kg}^{-1}$. The color shading in the area between the two grey straight lines shows the observed vertical velocity along the flight leg at 7200 m and the blue (green) colouring of the grey lines indicate observed cloud liquid (ice) exceeding $10^{-7} \text{ kg kg}^{-1}$. The black dashed lines show the location of the aircraft legs at 6900 m and 6780 m. Black contours indicate the topography. (b) Vertical cross-section through the wave cloud at 42.05° N (2100 UTC). The colour shading represents the modelled liquid water content, the contour lines with the hatching the modelled ice water content and the orange lines indicate isentropes. The horizontal lines show the projection of the flight path on the plane of the cross-section, where red colouring of the lines indicates observed cloudy conditions (condensed water content larger than $10^{-7} \text{ kg kg}^{-1}$). The grey area at the bottom of the plot shows the topography.

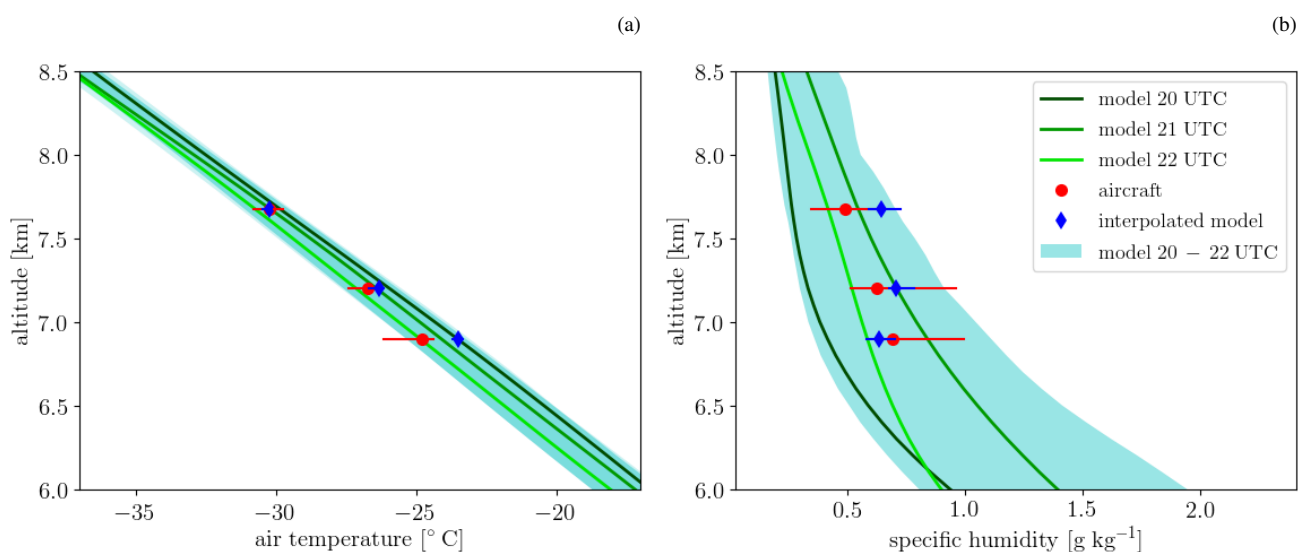


Figure 2. Comparison of upstream temperature (a) and specific humidity (b) profiles from the UM simulation and aircraft data. Upstream conditions from aircraft data are computed from the non-cloudy sections of the aircraft legs west of -105° E. Red circles indicate the mean value along these portions of the aircraft legs and the bars the variability. The model values are taken from the grid column closest to the average location of these upstream aircraft segments (green lines) at times between 2000 UTC and 2100 UTC, i.e. bracketing the time of the observations between ~ 2040 UTC and ~ 2120 UTC. The cyan shading shows the variability of temperature and specific humidity in this grid column for all output times between 2000 UTC and 2200 UTC. The blue diamonds and bars show the model data interpolated to the flight track and evaluated in the same way as the aircraft data.

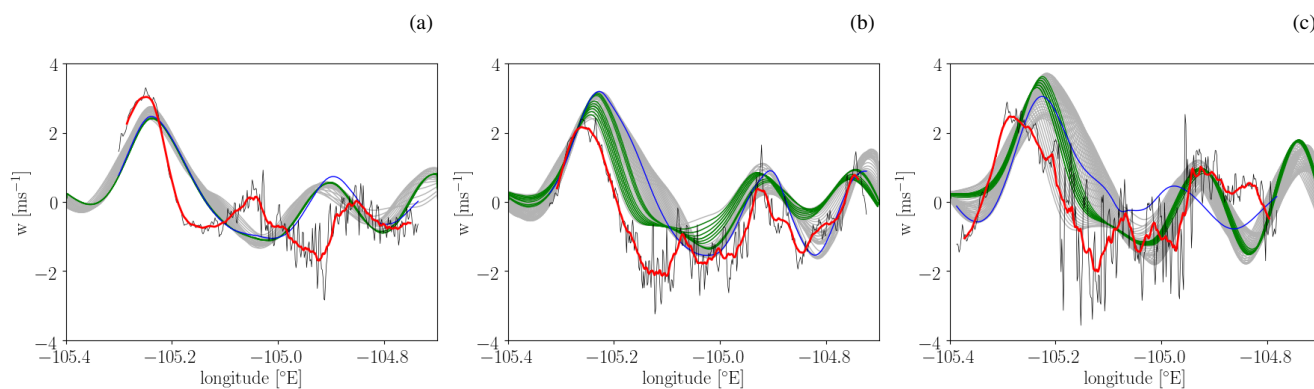


Figure 3. Vertical velocity along the flight legs at 7680 m (2120 UTC) (a), 7200 m (2100 UTC) (b) and 6900 m (2040 UTC) (c). The red solid line shows the aircraft data smoothed with a 20s moving average filter (full 1 Hz data shown by the thin black line). The blue line shows the modelled aircraft velocity interpolated to the aircraft track. The grey lines show the vertical velocity along tangents to the mean streamline (including a deviation corresponding to the deviation between the observed mean horizontal wind direction and the direction of the aircraft track), for which the peak vertical velocity exceeds 2.5 ms. This threshold was chosen to focus on the centre of the wave cloud only. The green line shows the tangent for which the Pearson correlation (including a lag of ± 20 s) with the observed vertical velocity is larger than 0.95. To account for the temperature bias of the model, model data is taken 200 m above the altitude of the flight track.

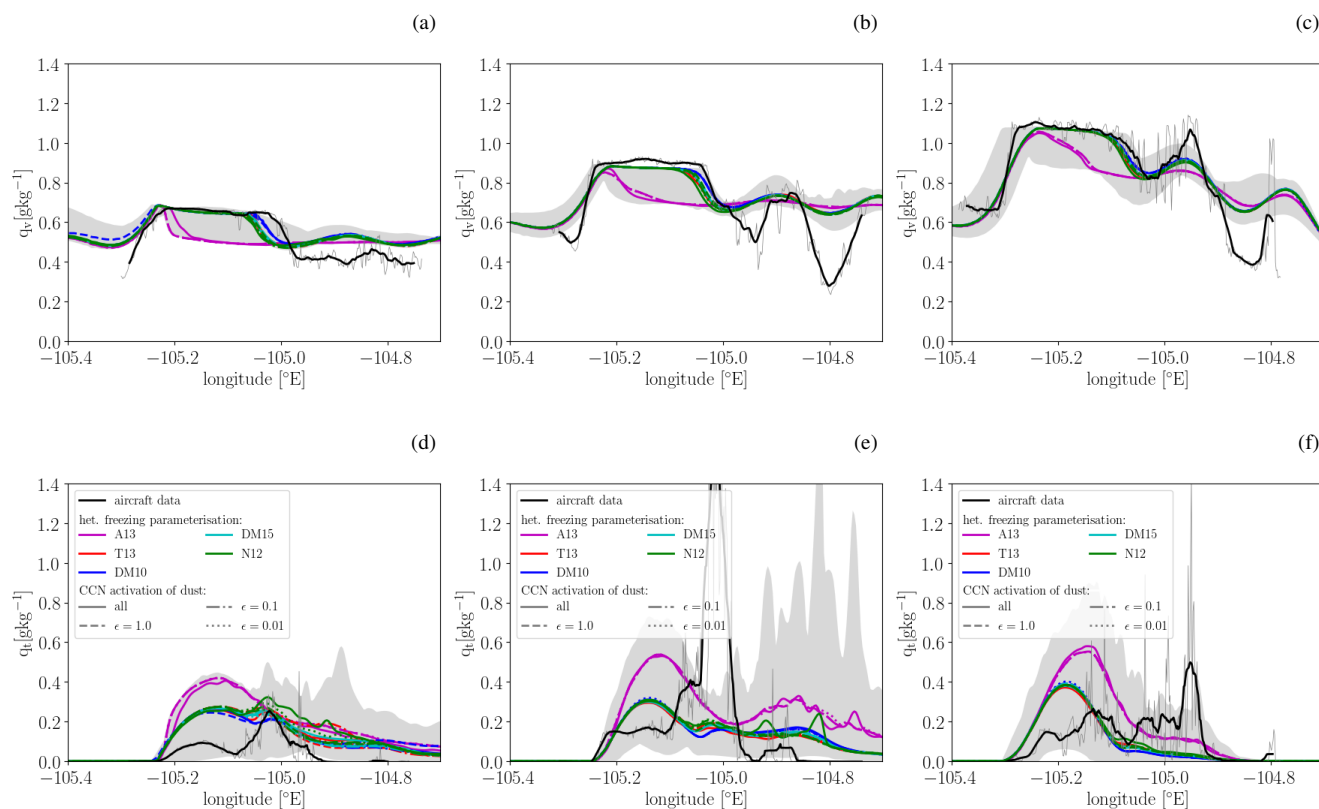


Figure 4. Comparison of specific humidity (a-c) and total condensation mass mixing ratio (d-f) for the three different flight legs. The flight legs are shown in the sequence of decreasing flight altitude from left to right. The thick black lines shows the smoothed aircraft data (thin black line shows 1 Hz data). Model data are interpolated to the same tangents of the mean streamlines as used in Fig. 3. The variability of the variables along all these hypothetical flight paths are shown by the grey shading, while the thick coloured lines show the median values for simulations. The different coloured lines represent with different ice nucleation schemes and different line styles indicate different assumptions on the amount of soluble material in the dust particles. The legend in panel (d) is valid for all panels.

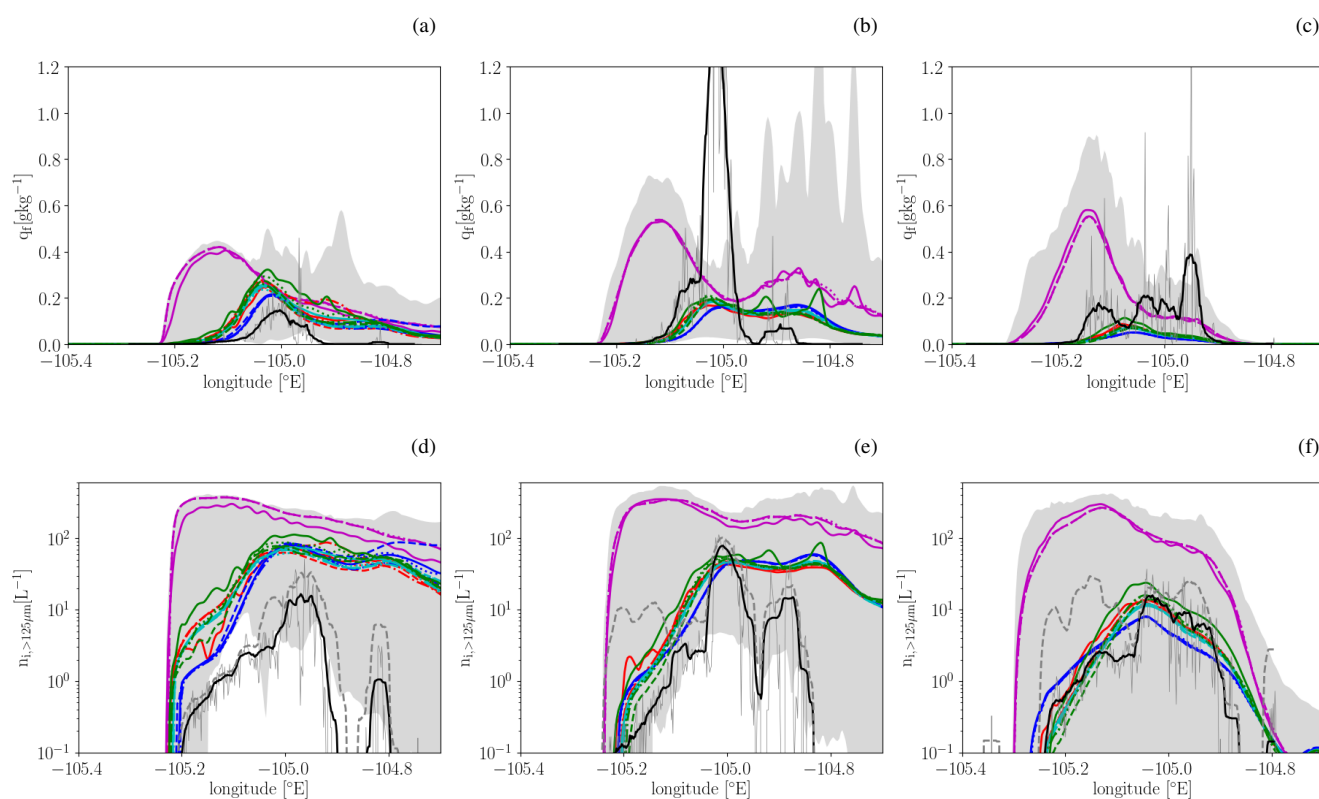


Figure 5. As Fig. 4 but showing the frozen hydrometeor mass mixing ratio (a-c) and ice crystal (d-f) number concentration. The data incorporates only crystals larger than $125\ \mu\text{m}$. The legend in Fig. 4 d is valid here as well.

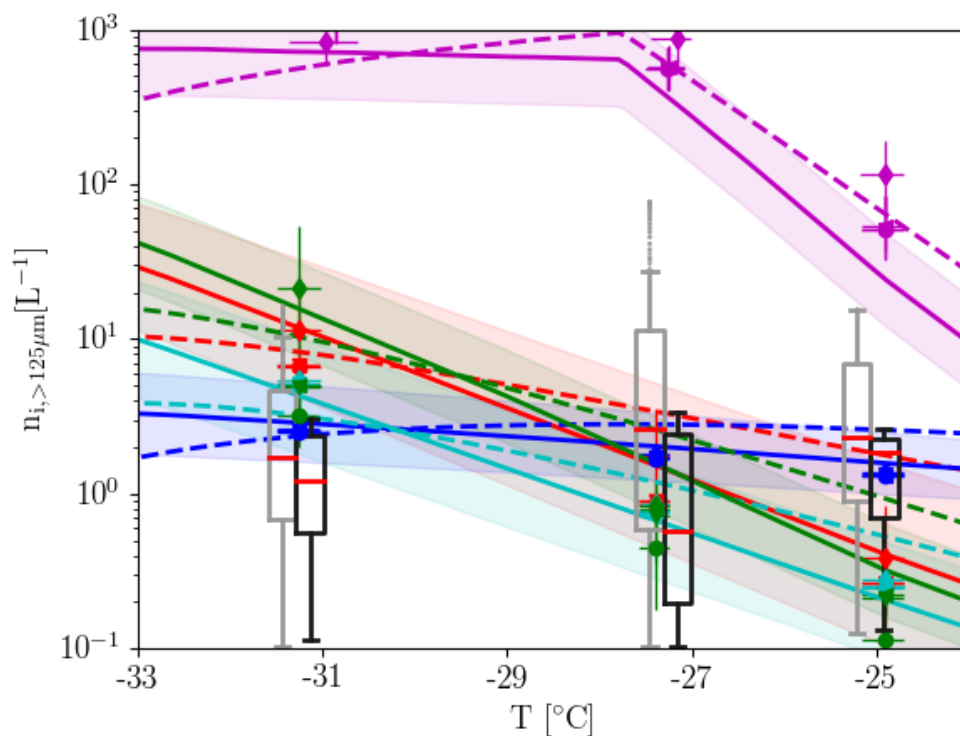


Figure 6. Temperature dependency of ice crystal number concentration against air temperature from observations (box-plots) and UM model simulations (symbols, colours represent simulations with different ice nucleation schemes according to legend in Fig. 4 a). Model data is interpolated to the hypothetical flight tracks and only considered in the first part of each flight leg, i.e. the updraft region. Observational data is also sub-sampled to include only data from the updraft region, which is shown in the black box-plots (grey box-plots show all data). The solid lines show the expected ice crystal number concentration based on ice nucleation only using the prescribed dust profiles. The colour shading illustrates the expected ice crystal number concentration for dust number concentrations within a factor 2 of the used profile, i.e. compatible with range observed upstream of the cloud. Assuming a linear decrease of the upstream dust concentration over the time period of the observations together with the ascending flight pattern results in expected ice crystal number concentration as shown by the dashed lines.

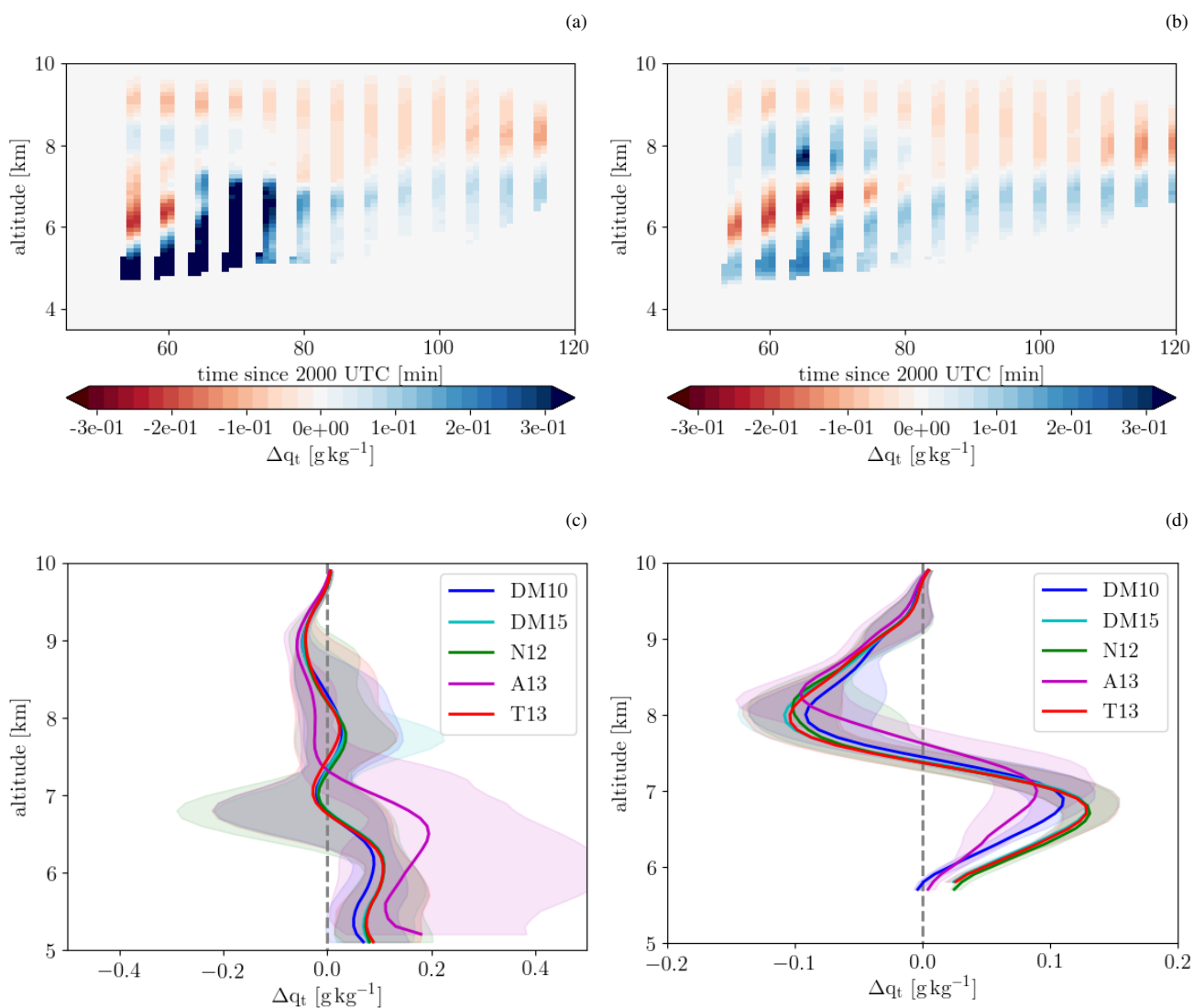


Figure 7. (a,b) Difference in total water mass mixing ratio Δq_t between -105.35°E (upstream) and -104.78°E (downstream) along backward trajectories for simulations using the A13 (a) and the (b) DM10 ice nucleation parameterisation, respectively. The plot shows values at 42.1°N , i.e. downstream of the centre of the wave cloud. The time on the abscissa indicate the arrival time of the trajectories at the downstream location. (c,d) Mean profiles of Δq_t for all simulations averaged between 2110 – 2130 UTC (c) and 2140 – 2200 UTC. The different colours correspond to simulations with different ice nucleation parameterisations, while the shading represents the temporal variability of the profiles. Note the travel time of the trajectories between the upstream and the downstream location is about 30 – 40 min.

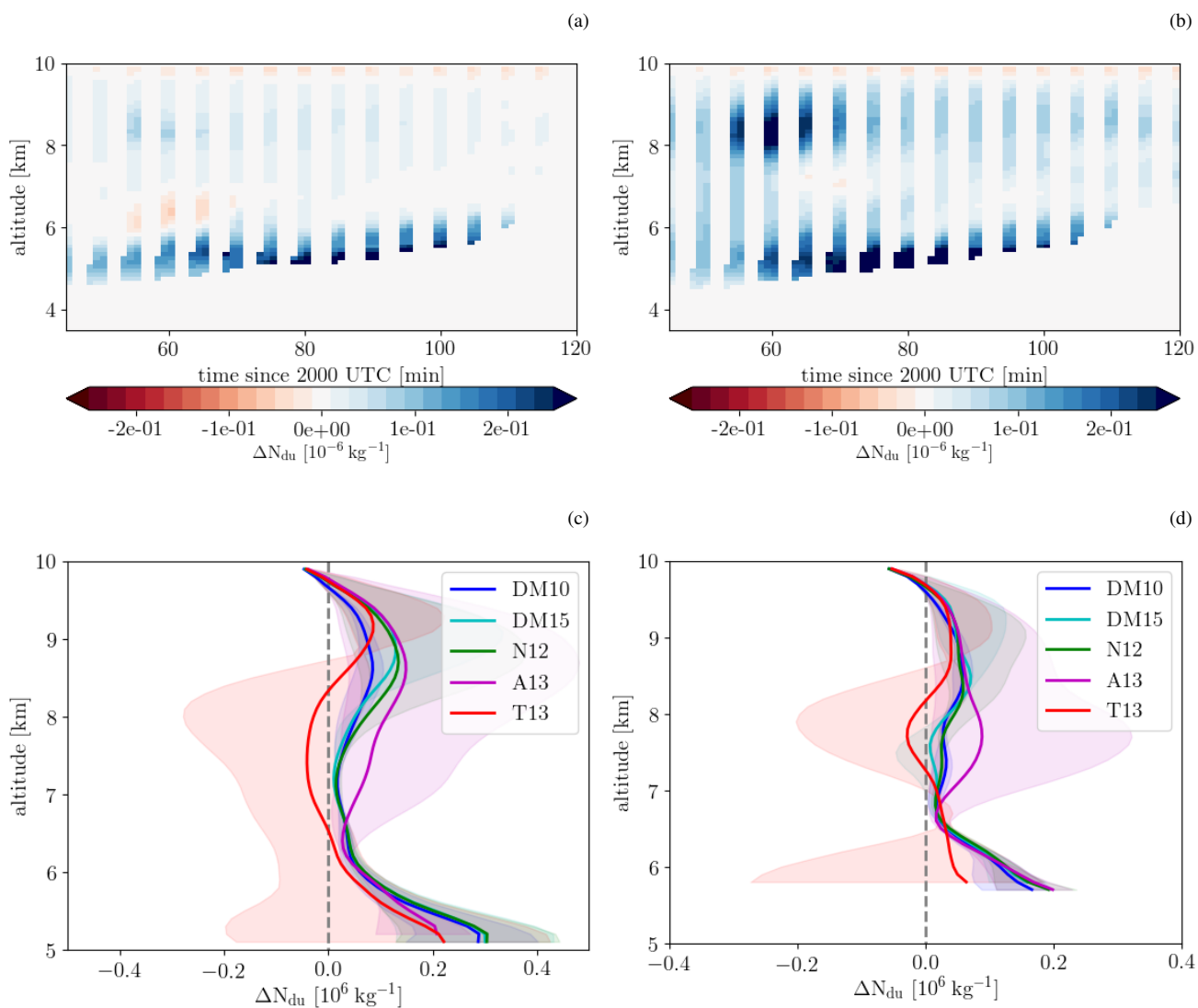


Figure 8. As Fig. 7 but showing the change in dust number concentration.

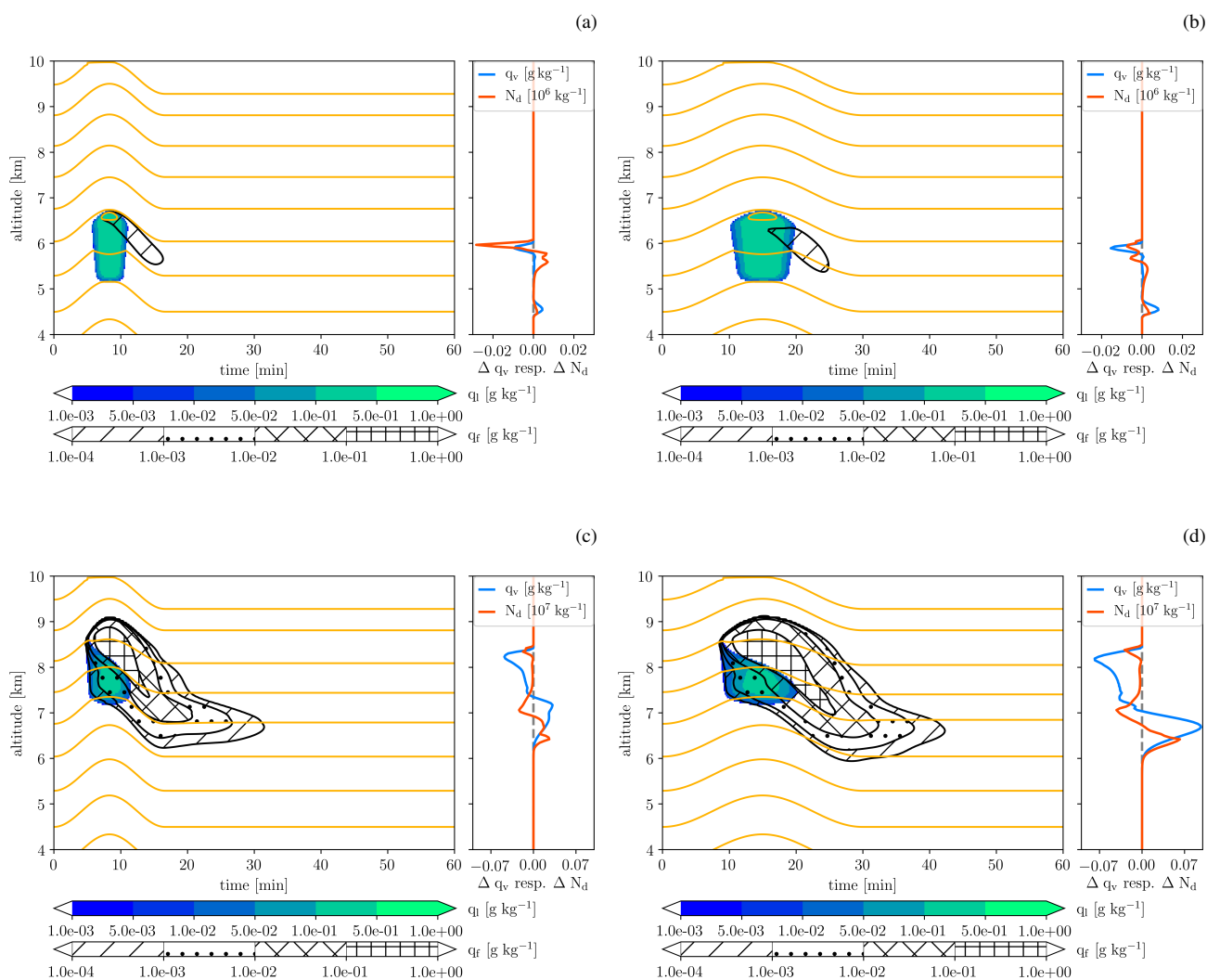


Figure 9. Wave clouds in the KiD-model. Simulations of waves with periods 1000 s (a, c) and 1800 s (b, d) are shown. The cloud top temperature is $-24\text{ }^{\circ}\text{C}$ in panels (a, b) and $-50\text{ }^{\circ}\text{C}$ in panels (c, d). The cloud droplet mass mixing ratio is indicated by the colour shading, ice and snow mass mixing ratio by the hatched contours and the isentropes by orange isolines with a spacing of 2 K. The small sub-panels show the difference in total water content (light blue line) and the dust number concentration (red line) between the upstream and downstream. Note the different units for the dust number concentration change in panels (a, b) and (c, d), respectively.

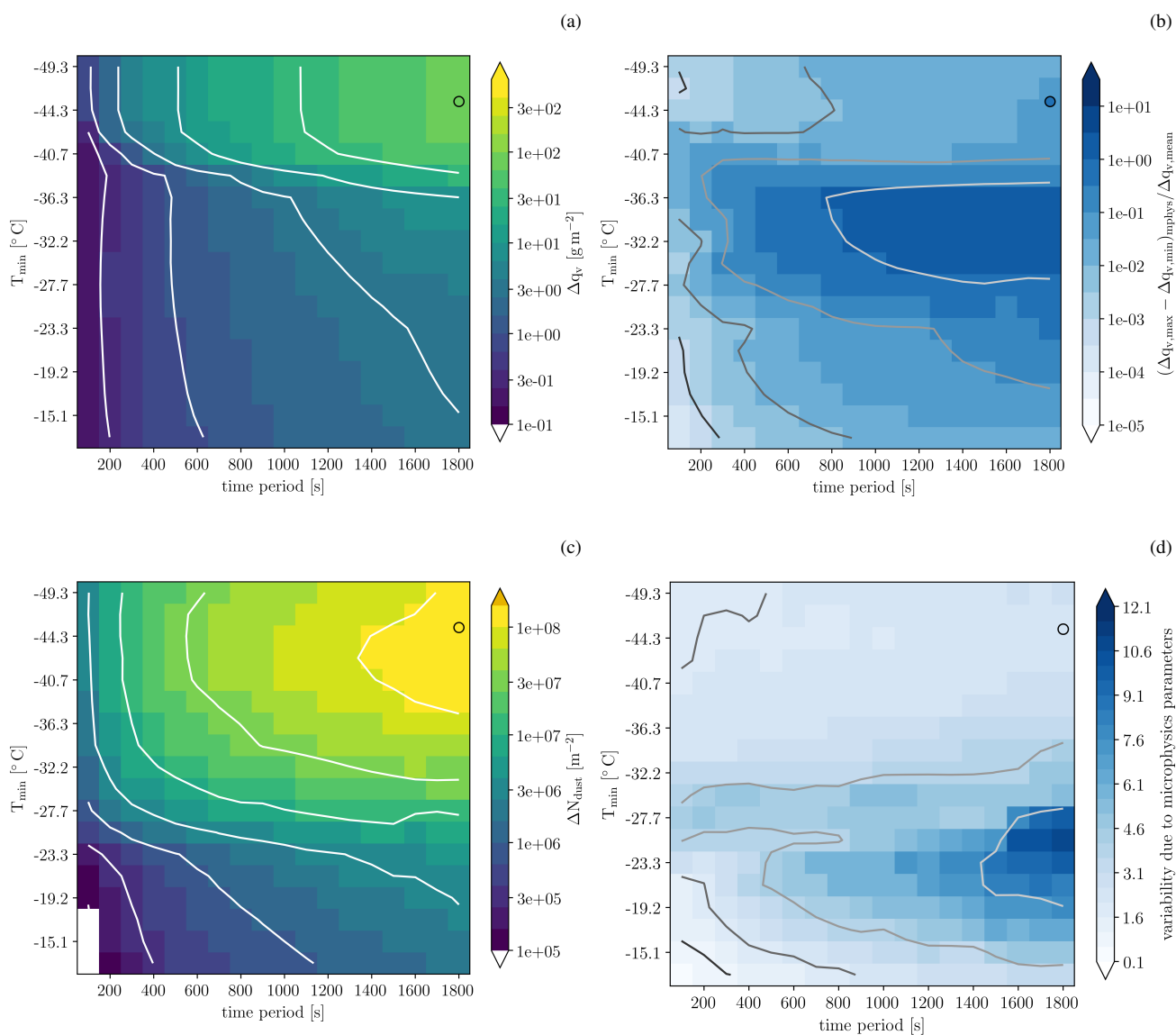


Figure 10. Sedimentation flux of water (a, b) and dust (c, d) across wave clouds with vertical extend z_c of 2500m and various cloud top temperatures (ordinate) as well as periods (abscissa). The panels in the left column show the mean value across simulations with all ice nucleations and soluble fraction assumptions, while the panels in the right column show the variability, i.e. $(\Delta_{\text{Lagr}q_t|_{\text{max}}} - \Delta_{\text{Lagr}q_t|_{\text{min}}}) / \Delta_{\text{Lagr}q_t|_{\text{mean}}}$ resulting from varying these.

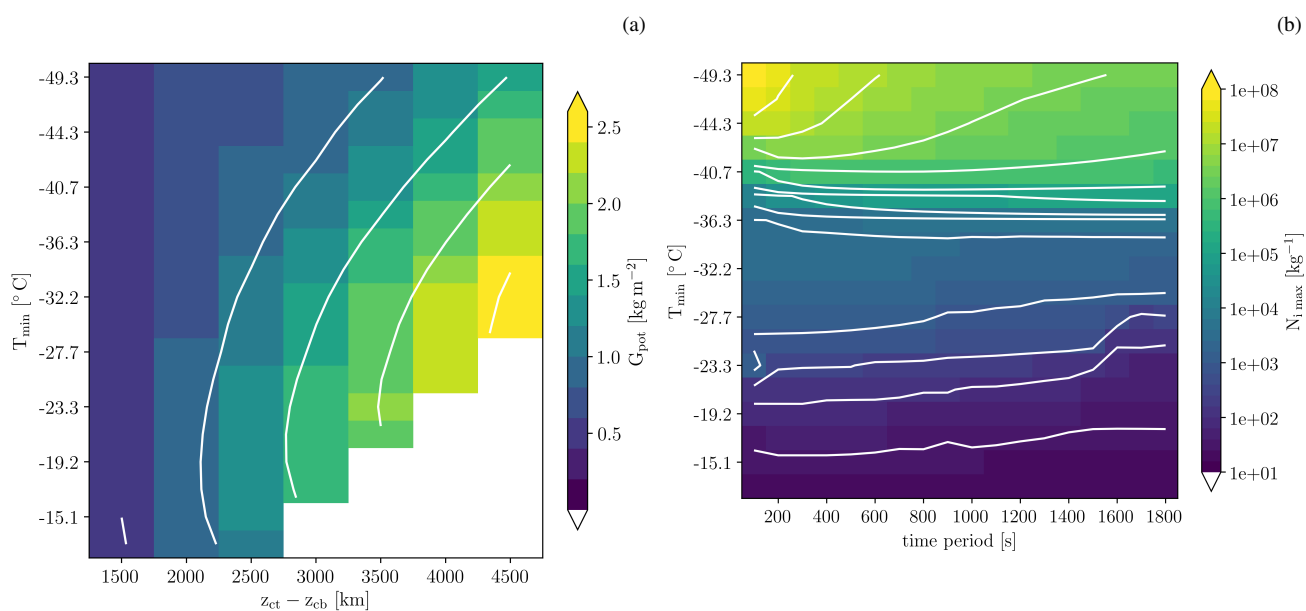


Figure 11. (a) Potential condensate G_{pot} as a function of cloud thickness and cloud top temperature. (b) Maximum ice crystal concentration $n_{i,\text{max,Lagr}}$ as a function of wave period and cloud top temperature for clouds with a thickness of 2 km. $n_{i,\text{max,Lagr}}$ is the maximum integrated ice crystal formation rate, including homogeneous and heterogeneous freezing, along any trajectory through the wave cloud.

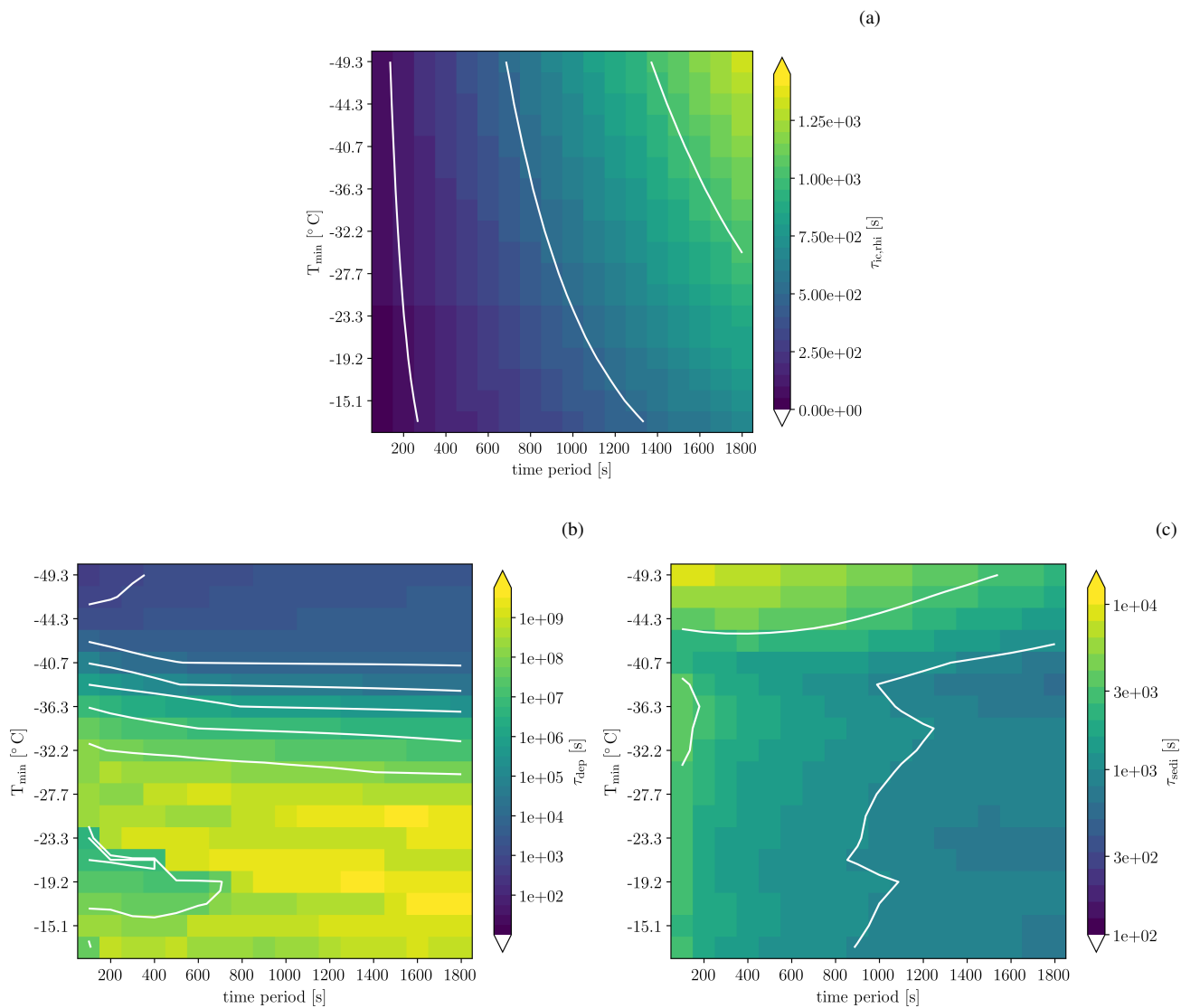


Figure 12. Lagrangian estimates of (a) the in-cloud residence timescale τ_{ic} , (b) the deposition timescale τ_{dep} and (c) the sedimentation timescale τ_{sed} . Results are shown for simulations with a cloud thickness of 2 km.

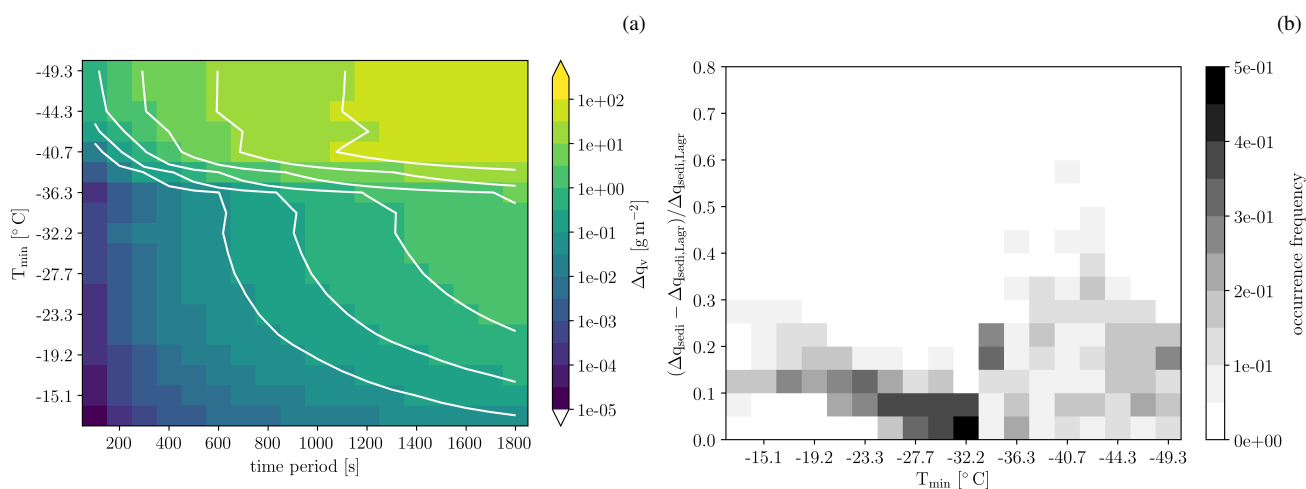


Figure 13. (a) Sedimentation flux of water predicted using equations 3 to 7 across wave clouds with vertical extent z_c of 2500 m, the DM10 heterogeneous freezing parametrisation, and various cloud top temperatures (ordinate) as well as periods (abscissa). (b) Normalised difference between sedimentation flux predicted by the conceptual model and the full KiD model for different cloud top temperatures. The data shown in (b) includes the full simulations set with all cloud top temperature, wavelength, and cloud thickness specified in section 2.3.